

The Stanford VI-E Reservoir: A Synthetic Data Set for Joint Seismic-EM Time-lapse Monitoring Algorithms

Jaehoon Lee and Tapan Mukerji
Department of Energy Resources Engineering
Stanford University

Abstract

A large-scale data set including time-lapse (4D) elastic attributes and electrical resistivity is generated with the purpose of testing algorithms for reservoir modeling, reservoir characterization, production forecasting, and especially joint time-lapse monitoring using seismic as well as electromagnetic data.

The Stanford VI reservoir, which was originally created by Castro et al. (2005), is a three-layer prograding fluvial channel system, and its structure corresponds to an asymmetric anticline with axis $N15^{\circ}E$. The reservoir provides an exhaustive data set (6 million cells) of petrophysical properties, seismic attributes, as well as time-lapse seismic data. Due to the need of testing field management algorithms using time-lapse electromagnetic and seismic data, several extensions and modifications are incorporated into an updated version of the data set, named as Stanford VI-E reservoir.

Archie's method (1942) and Waxman-Smits model (1968) are applied to create electrical resistivity for sand and shale facies respectively. Also, the rock physics models for seismic velocities are improved to give more realistic 4D seismic data. Flow simulation with different fluids within facies is performed to obtain the changes in saturation after oil production. Based on the result of the flow simulation, electrical resistivity and elastic attributes are calculated at different times during production.

Introduction

Reservoir management is a critical decision-making procedure throughout the life cycle of oil and natural gas fields in order to manage the behavior of hydrocarbon and hence maximize its production and recovery. More efficient management can be achieved by increasing the accuracy of reservoir characterization. However, even though the reservoir is reasonably characterized and well understood, its state and contents are changing as it is depleted. Therefore, continuous data gathering and monitoring are necessary to update the current condition of the reservoir.

Time-lapse (4D) seismic monitoring has been used to keep track of changes due to production in many fields (e.g., Tura and Lumley, 1999; Landrø, 2001; Lumley et al., 2003). It involves multiple 3D seismic measurements for the same area at different times during production. The images generated by 4D seismic data can help to monitor fluid flow in reservoirs and reveal spatial and temporal variations in fluid saturation, pressure, and temperature if their changes produce observable differences in seismic attributes. In recent years, electromagnetic imaging techniques, such as cross-well electromagnetic (Alumbaugh and Morrison., 1995; Wilt et al., 1995) or controlled-source electromagnetic methods (CSEM) (Constable and Cox, 1996; MacGregor et al., 2001) have been attempted as key tools for reservoir monitoring. Electromagnetic technology can provide electrical resistivity distribution in reservoirs and thus specify fluid saturation and reservoir structure because of the excellent contrast of resistivity between brine-filled zones and hydrocarbon-filled zones.

A hydrocarbon reservoir is a complex earth system delineated by various types of characteristics, for example geological, petrophysical, geophysical, and fluid dynamic properties. It is, however, not possible to access and measure all the truth about the reservoir due to its expense and technological limitations. Therefore, synthetic data are very useful to enable extensive testing of any proposed algorithms for reservoir modeling, characterization, forecasting, and management before applying them to real cases.

Over the past few decades, the Stanford Center for Reservoir Forecasting (SCRF) created several synthetic reservoirs with the purpose of testing algorithms suggested by the research group of SCRF, such as the Stanford V (Mao and Journel, 1999) and the Stanford VI reservoir (Castro et al., 2005). Especially, the Stanford VI reservoir exhibits a smooth structure with more realistic dimensions for present-day models and provides exhaustive sampling of petrophysical properties and seismic attributes originally for the evaluation of upscaling and downscaling methods. Additionally, it contains 4D seismic data generated by using a flow simulator.

Although the Stanford VI has been widely used for many researches in SCRF, this data set is not enough to be used for 4D seismic monitoring algorithms due to imperfection in the rock physics models. Moreover it does not contain electrical resistivity or conductivity for electromagnetic imaging algorithms. Therefore, the Stanford VI-E reservoir, an updated version of the data set, is generated with improved rock physics models, electrical resistivity, and more realistic fluid simulation in order to study field management algorithms using time-lapse electromagnetic and seismic data.

This report describes the workflow used for building the Stanford VI-E reservoir, as well as a detailed description of each step.

Workflow for Stanford VI-E

The workflow for creating the Stanford VI-E reservoir data set is summarized in Figure 1. Basically, this workflow is similar to the one provided by Castro et al., (2005) but several steps are modified and added. In the workflow, gray boxes indicate that the same data of the Stanford VI are used in building the Stanford VI-E reservoir. The updated reservoir properties are shown in blue boxes and the newly created properties are presented in red boxes.

The Stanford VI-E reservoir uses the same structure and stratigraphy with the Stanford VI reservoir. In the Stanford VI, the facies model was created by using the commercial software **SBED** and the multiple-point geostatistics algorithm **SNESIM**. Porosity was simulated using the sequential Gaussian simulation algorithm **SGSIM** and then permeability was co-simulated with co-located porosity by the **COSGISM** algorithm. The Stanford VI-E maintains the porosity model simulated in the Stanford VI but adjusts the permeability model to induce fluid to flow mostly through sandstones.

P-wave and S-wave velocities are obtained from the simulated porosity using well known rock physics models. Elastic attributes; acoustic impedance, S-wave impedance, elastic impedance, Lame's parameters, and Poisson's ratio are computed using mathematical expressions. Electrical resistivity model is newly generated by using Archie's method (1942) for sands and Waxman-Smits model (1968) for shaly-sands.

In order to obtain the change in fluid saturation, flow simulation using the commercial software **ECLIPSE** is conducted for the initial state of the Stanford VI-E reservoir, which is assumed that all the sand facies are oil saturated (residual brine saturation condition; $S_{brine} = 0.15$ and $S_{oil} = 0.85$) while all the shale facies are fully brine saturated ($S_{brine} = 1$).

Subsequently, all the elastic and electromagnetic properties are computed at different times during oil production in the Stanford VI-E reservoir based on the flow simulation result. In the Stanford VI-E, all the data are represented at the point scale (geostatistical scale), so any filtering and smoothing are not applied to create the seismic and electromagnetic scale data. This can give flexibility in choosing forward modeling methods or using just a small part of the reservoir.

The following sections of this report explain the details of each step of the workflow presented in Figure 1.

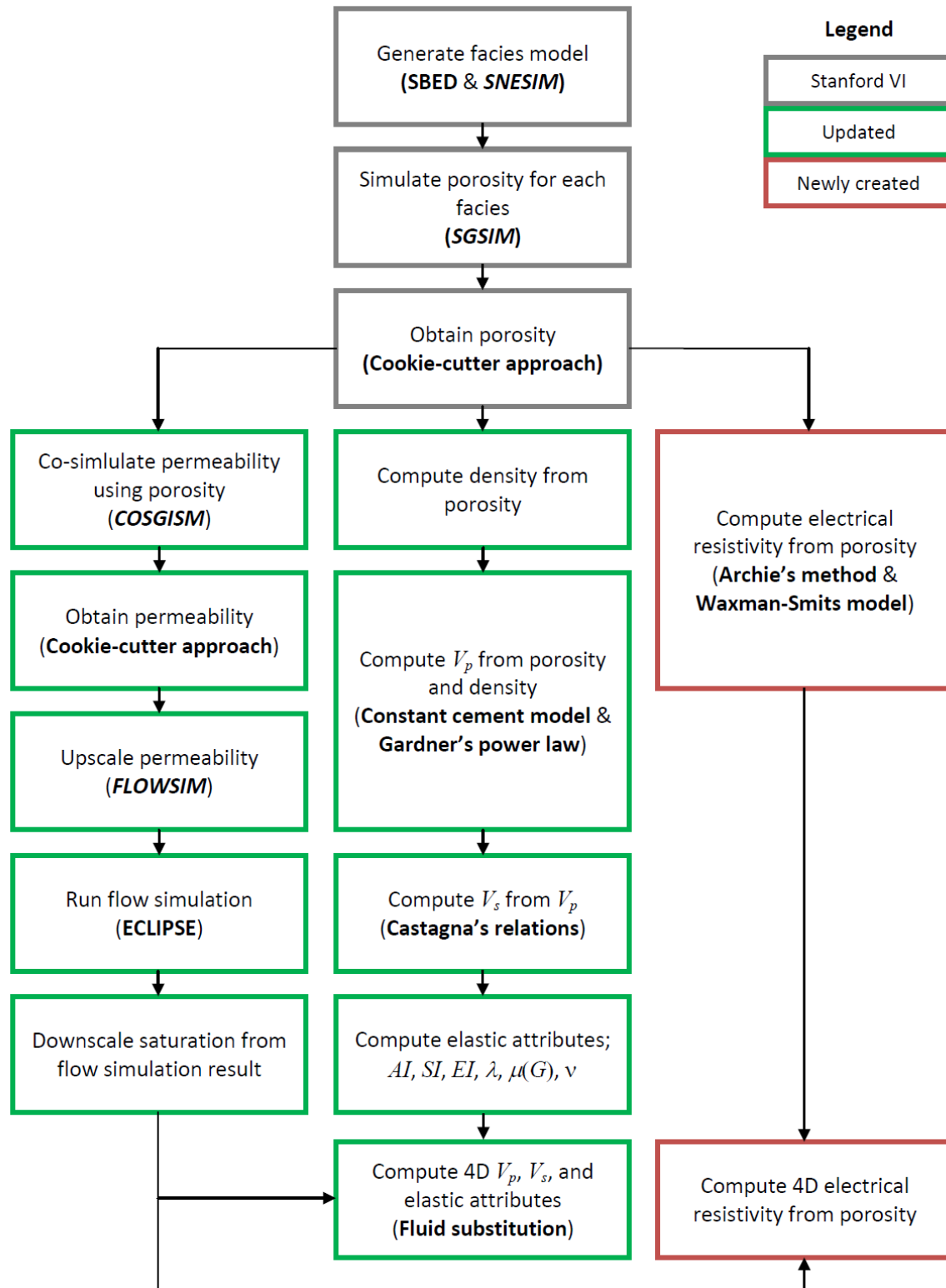


Figure 1. Workflow used to build the Stanford VI-E reservoir. Gray boxes mean that the same data of the Stanford VI are used in the Stanford VI-E. Blue boxes show the updated data from the Stanford VI and red boxes indicate the newly created data in the Stanford VI-E.

Stanford VI Reservoir

The Stanford VI-E reservoir is generated based on the structure, stratigraphy, and porosity of the Stanford VI reservoir. Although the permeability is changed for realistic flow behavior, we did not conduct a new co-simulation so it will be explained in this section.

Structure and Stratigraphy

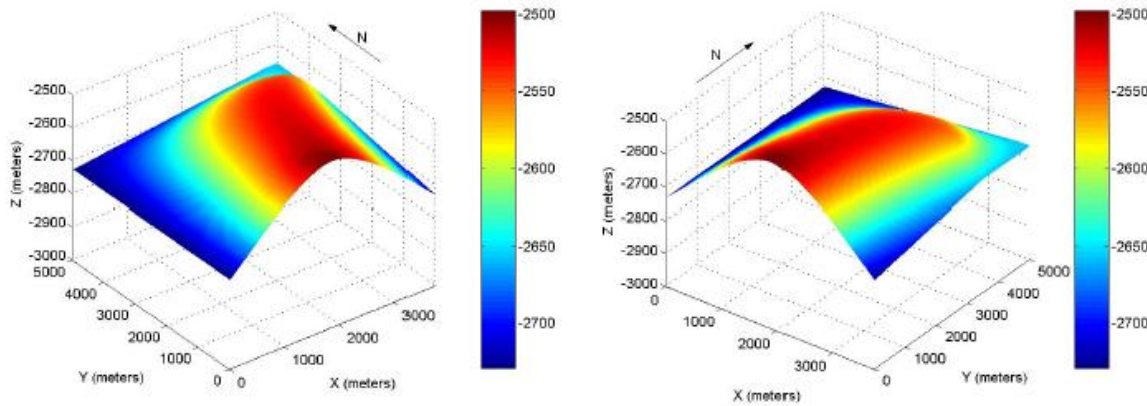


Figure 2. Perspective view of the Stanford VI top surface from SW (left) and from SE (right). The color indicates the depth to the top surface. (Castro et al., 2005).

The structure of the Stanford VI reservoir is an asymmetric anticline, which is a classical oil trap, with axis $N15^{\circ}E$. Figure 2 shows the structure and depth of the top surface of the reservoir. The structure has a different dip on each flank and the magnitude of the dip decreases slowly towards the northern part of the reservoir. The maximum dip of the structure is 8° . The shallowest depth of the top surface is about $2,500m$ and the deepest one is $2,730m$.

The Stanford VI reservoir is represented as a three-dimensional regular stratigraphic model with $150 \times 200 \times 200$ cells. The dimensions of the cell are $25m$ in the horizontal directions (x and y) and $1m$ in the vertical direction (z). So the size of the reservoir is $3,750m$ along the east-west axis and $5,000m$ along the north-south axis with thickness of $200m$. It consists of three layers and each layer is respectively $80m$, $40m$, and $80m$ thick.

Stratigraphically, the Stanford VI reservoir corresponds to a fluvial channel system prograding into the basin located toward the north of the reservoir. Deltaic deposits (*layer 3*) were formed first and meandering channels (*layer 2*) and then sinuous channels (*layer 1*) were deposited in this fluvial channel system. The *layer 1* and *2* are represented by four facies: *floodplain* (shale deposits), *point bar* (sand deposits that occur along the convex inner edges of the meanders of

channels), *channel* (sand deposits), and *boundary* (shale deposits). The *layer 3* consists of two facies: *floodplain* and *channel*. In order to model the stratigraphy of the Stanford VI, the commercial software **SBED** was used for the *layer 1* and *2* while the multiple-point statistics algorithm **SNESIM** (Strebelle, 2000; Strebelle, 2002) was applied for the *layer 3*. Refer to the original paper about the Stanford VI (Castro et al., 2005) for the detailed methodologies and model parameters. Figure 3 shows the resulting stratigraphic (facies) model.

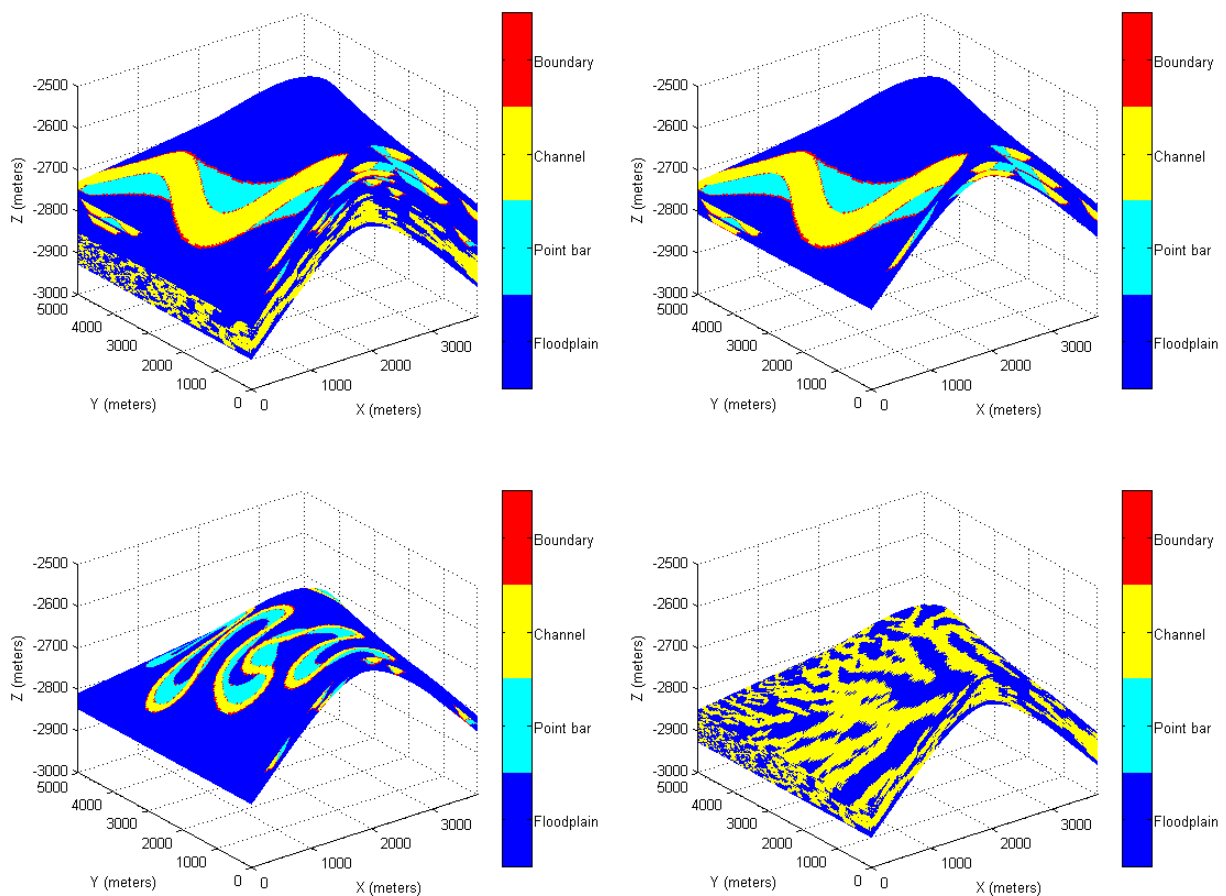


Figure 3. Stratigraphic model of the Stanford VI (top-left); *layer 1* (top-right), *layer 2* (bottom-left), and *layer 3* (bottom-right). (Modified from Castro et al., 2005)

Porosity

Porosity was independently simulated for each facies by assuming that the entire reservoir consists of only one facies. The sequential Gaussian simulation algorithm **SGSIM** conditioned to reference target distributions and variograms was used in the Stanford VI reservoir. The details

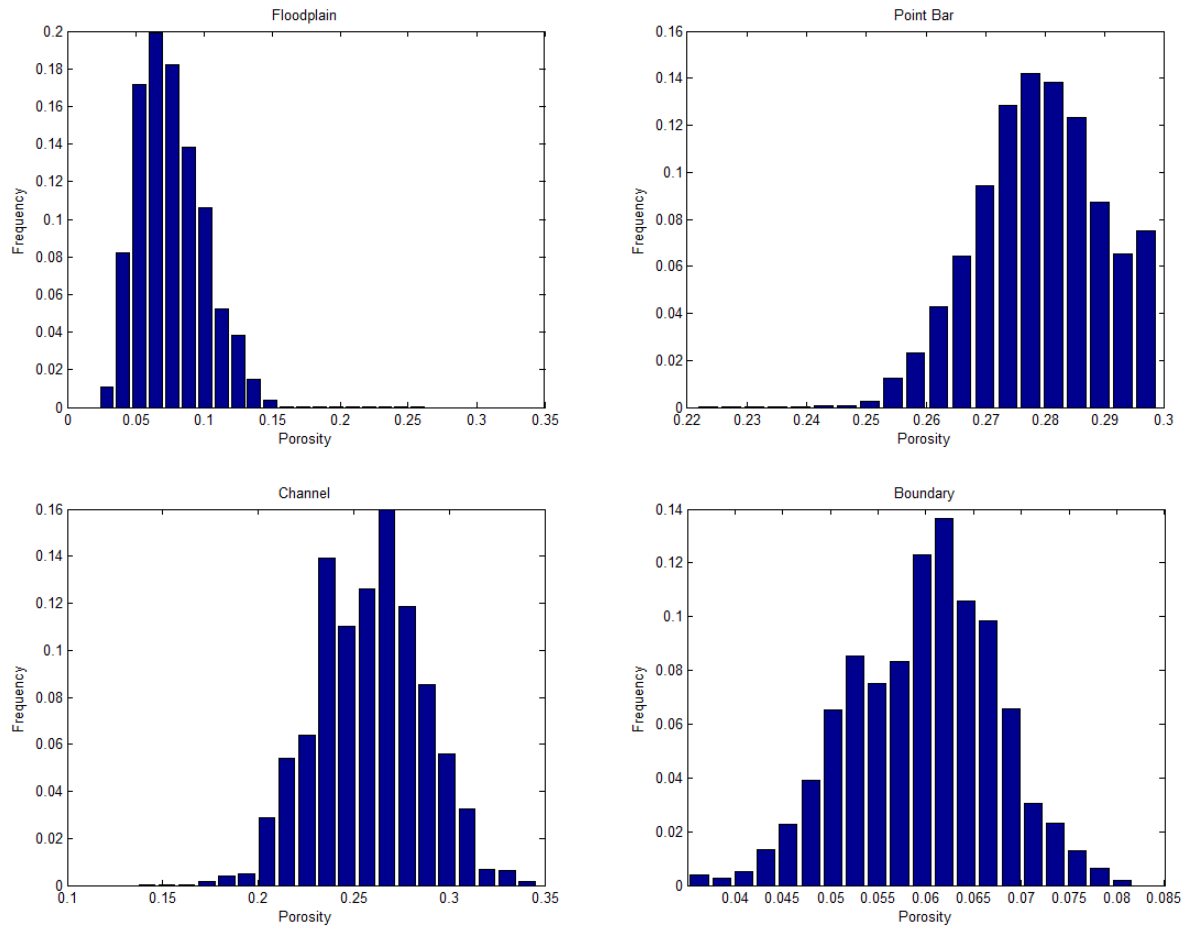


Figure 4. Histogram of porosity for each facies in the Stanford VI.

of the target distributions and variograms used for the simulation can be found in the original paper (Castro et al., 2005). After the porosity for each facies was simulated, a cookie-cutter approach, in which porosity was selected from the simulated porosity of the facies corresponding to the stratigraphic model, was applied to create the porosity model for the Stanford VI. Figure 4 shows the histogram of the porosity in the Stanford VI and the resulting porosity model is presented Figure 5.

Permeability

In the Stanford VI reservoir, the logarithm of permeability was co-simulated using the simulated porosity as secondary information with a linear correlation coefficient of 0.7 between two variables. The sequential Gaussian co-simulation algorithm **COSGSIM** was applied with a Markov-type model (Almeida and Journel, 1994) instead of a full model coregionalization. Permeability was also simulated independently for each facies and then the cookie-cutter

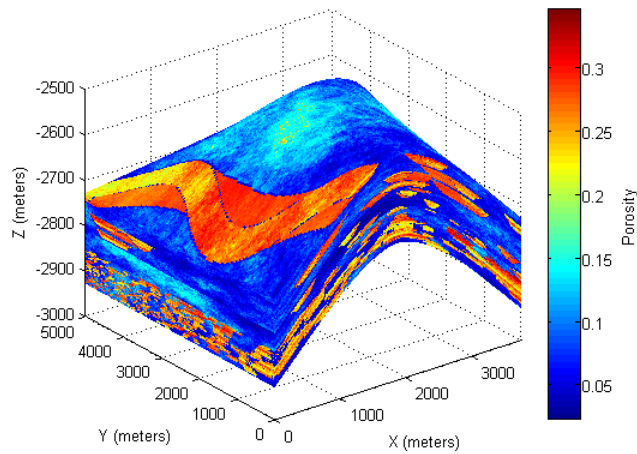


Figure 5. Porosity model of the Stanford VI. (Castro et al., 2005)

approach was used to merge the permeability simulated for each facies into a single permeability model.

The reference target distributions of permeability for the co-simulation were obtained by transforming the target distributions of porosity using the Kozeny-Carman relation (Carman, 1937):

$$\kappa = \frac{1}{72\tau} \frac{\phi^3}{(1-\phi)^2} d^2 \quad (1)$$

where κ is permeability, τ is tortuosity (assumed as 2.5), ϕ is porosity, and d is the diameter of particles (assumed that $180\mu m$ for sand facies and $130\mu m$ for shale facies). However, the assumed particles sizes are both typical values of fine sand.

Furthermore, Bourbié et al. (1987) experimentally investigated the Kozeny-Carmen relation and suggested that a more general form of the relation:

$$\frac{\kappa}{d^2} \propto \phi^n \quad (2)$$

with the factor $n = 4$ or 5 for natural materials and even larger than 7 for low-porosity materials. And they observed that the Kozeny-Carmen relation with $n = 3$ is appropriate only for very clean sandstone. Also, Mavko and Nur (1997) showed that percolation porosity, which is usually large for shale, should be considered in order to retain $n = 3$ when the Kozeny-Carmen relation

is used. Percolation porosity is the threshold where the remaining porosity is disconnected and does not contribute to flow.

As a result, the simulated values for the permeability of shale facies (*floodplain* and *boundary*) are much higher than typical values of shale permeability (see Figure 7). Therefore, the shale facies in the Stanford VI significantly contributes to the flow of hydrocarbon in flow simulation rather than works as a flow barrier that is usually the case in real reservoirs.

Thus, in order to make the flow behavior more realistic in the Stanford VI-E reservoir, the shale permeability in the Stanford VI is divided by the factor of 100 rather than constructing a reasonable target distribution and co-simulating permeability again. Figure 6 shows the histogram of permeability for the Stanford VI-E reservoir. Figure 7 compares the permeability models for the Stanford VI and Stanford VI-E reservoir.

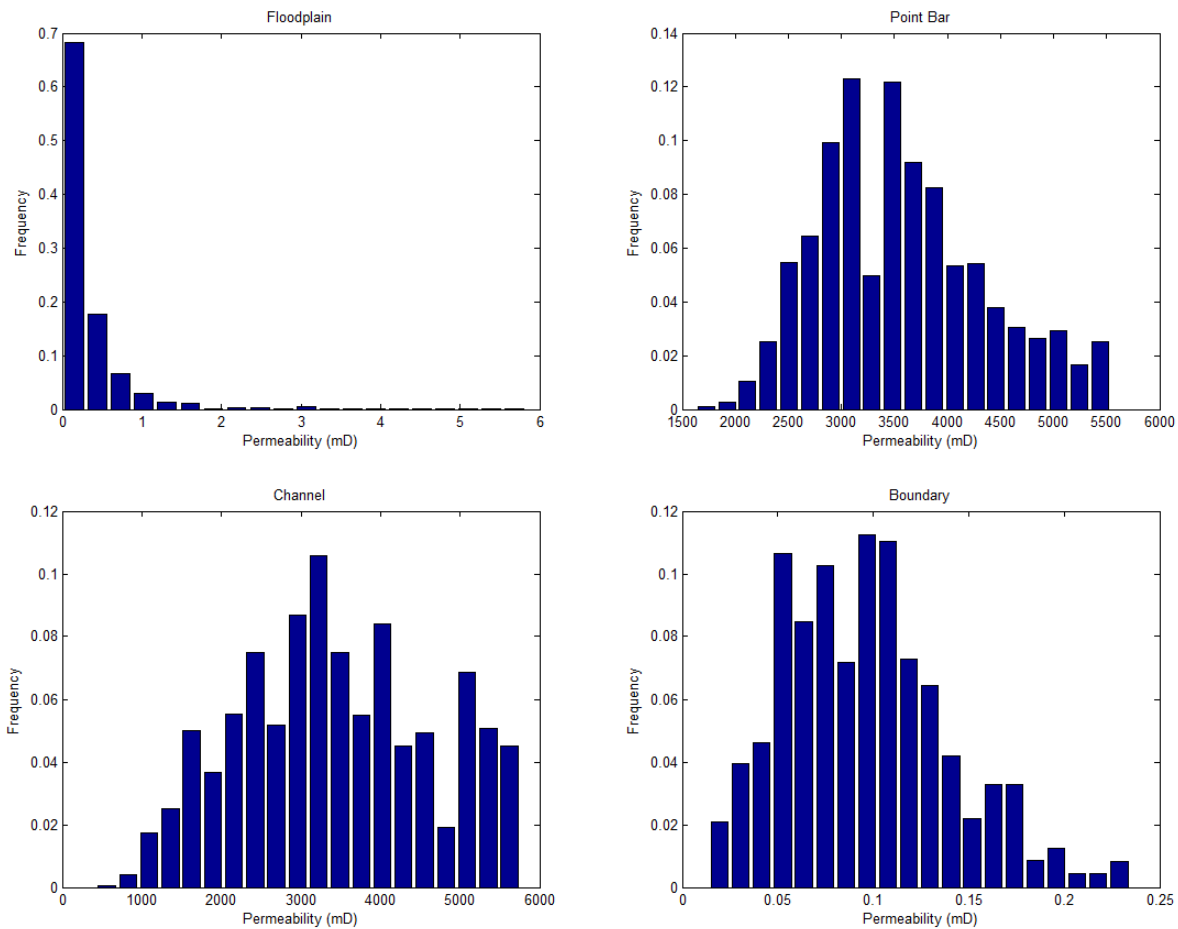


Figure 6. Histogram of porosity for each facies in the Stanford VI-E.

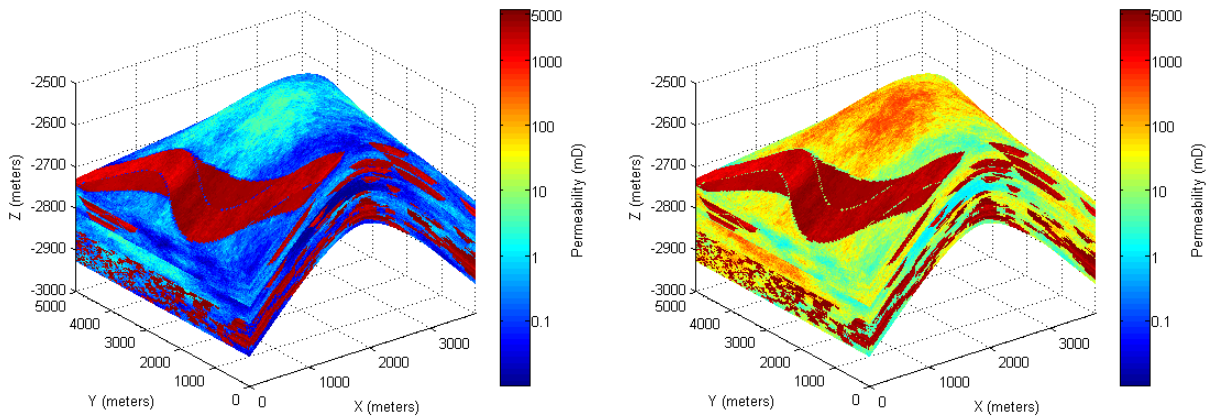


Figure 7. Permeability models of the Stanford VI-E (left) and Stanford VI (right)

Petrophysical Properties

From the facie and porosity of the Stanford VI, we create the petrophysical properties; density, P-wave velocity, and S-wave velocity for the Stanford VI-E.

Density

The bulk density of rock is a simple volumetric average of the densities of rock constituents and, thus, can be calculated by using the simulated porosity ϕ as follows:

$$\rho = \phi \rho_f + (1-\phi) \sum_{i=1}^N f_{m(i)} \rho_{m(i)} \quad (3)$$

where ρ_f is the density of pore fluids, $f_{m(i)}$ is the volume fraction of the mineral constituent i within the solid phase of the rock, and $\rho_{m(i)}$ is the density of the mineral constituent i .

Table 1 shows the fractions of rock minerals for each facies and Table 2 presents the density and elastic properties of minerals used in the Stanford VI-E. The mineral density and fractions of shale facies are different with those of the Stanford VI not to violate the Hashin-Shtrikman bounds (Hashin and Shtrikman, 1963).

The Stanford VI-E has brine and oil as its pore fluids. The properties of brine and oil are obtained from Batzel and Wang (1992). Mostly based on empirical measurements, Batzel and Wang (1992) summarized important properties of reservoir fluids such as brine, oil, gas, and live oil as a function of pressure, temperature, and composition. In the Stanford VI-E, the brine and oil properties for pore pressure of 20MPa and temperature of 85°C are used. Table 3

Table 1. Mineral fractions of each facies in the Stanford VI-E

Mineral \ Facies	Floodplain	Point bar	Channel	Boundary
Clay	0.85	0.0	0.0	0.9
Quartz	0.15	0.7	0.65	0.1
Feldspar	0.0	0.2	0.2	0.0
Rock fragments	0.0	0.1	0.15	0.0

Table 2. Density and elastic properties of minerals (source: Mavko et al., 2009)

Mineral \ Property	Density (g/cc)	Bulk modulus, K (GPa)	Shear modulus, G (GPa)
Clay	2.5	21	9
Quartz	2.65	36.6	44
Feldspar	2.63	75.6	25.6
Rock fragments	2.7	80	20

Table 3. Brine and oil properties and composition (source: Batzel and Wang, 1992)

Property Fluid \	Density (g/cc)	Bulk modulus, K (GPa)	Salinity (NaCl ppm)	Gravity (API)	Gas-oil ratio (L/L)	Gas specific gravity
Brine	0.99	2.57	20,000	-	-	-
Oil	0.70	0.50	-	25	200	0.7

presents the brine and oil properties and the composition assumed for obtaining those properties from the Batzel and Wang relations.

As the initial state of the Stanford VI-E reservoir, it is assumed that all the sand facies (*point bar* and *channel*) are oil saturated (residual brine saturation condition; $S_{brine} = 0.15$ and $S_{oil} = 0.85$) while all the shale facies (*floodplain* and *boundary*) are fully brine saturated ($S_{brine} = 1$). When two fluids are present with different partial saturation, they can be replaced with a single effective fluid to model the state of two phases. The density of the effective fluid is computed with the following mixing formula:

$$\rho_f = \sum_{i=1}^2 S_{f(i)} \rho_{f(i)} \quad (4)$$

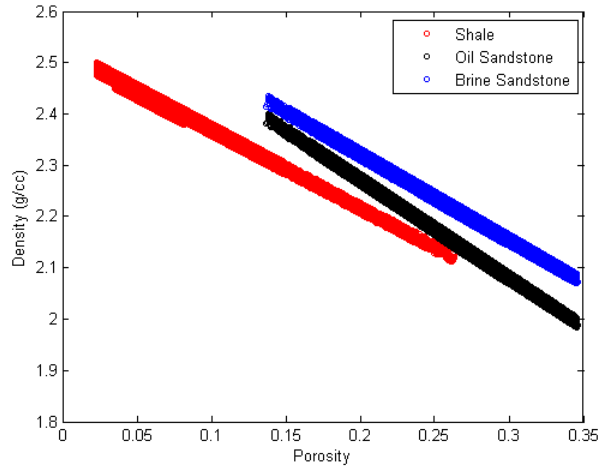


Figure 8. Porosity vs. density in the Stanford VI-E.

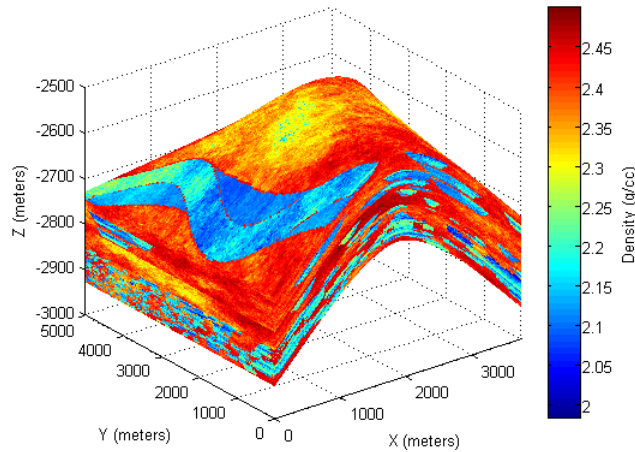


Figure 9. Density model for the initial state of the Stanford VI-E.

where ρ_f is the effective density of the fluid mixture, $\rho_{f(i)}$ is the density of the individual fluid i , and $S_{f(i)}$ denotes its saturation.

Since the density is mathematically calculated, its relationship with the porosity simply shows only one continuous function for each facies. Therefore, 0.5% of uniform random variability is added to the simulated density in order to give some scatter to the synthetic data. Figure 8 presents the crossplot between the porosity and density for the initial and brine-saturated conditions and Figure 9 shows the density model for the initial state of the Stanford VI-E reservoir.

P-wave and S-wave Velocities

P-wave Velocity

Numerous researchers have suggested the relationships between seismic velocity and porosity based on laboratory experiments (e.g., Wyllie et al., 1956; Raymer, et al., 1980; Tosaya and Nur, 1982; Han et al., 1986; etc.) or theoretical models (e.g., Dvorkin et al., 1994, Dvorkin and Nur, 1996) and all of them are constructed for certain rock types or depositional conditions. Therefore, a rock physics model for creating seismic velocity from porosity should be carefully selected among them.

Avseth et al. (2000) suggested the constant cement model for poorly-cemented sandstones by combining a contact cementation theory (Dvorkin et al., 1994) with the Hashin-Shtrikman lower bound (Hashin and Shtrikman, 1963). Since the Stanford VI-E reservoir is a prograding fluvial channel system which does not exhibit a wide range of depths, we can assume that the porosity is controlled more by sorting than cementing or diagenesis. Therefore, the constant cement model is applied to create the P-wave velocity (V_p) for sand facies in the Stanford VI-E.

The constant cement model is a theoretical model that predicts the bulk modulus K and shear modulus G for dry sandstone with constant amount of cement deposited at grain surface. With the assumption of homogeneous, isotropic, and elastic media, the P-wave velocity of seismic waves is given by

$$V_p = \sqrt{\left(K + \frac{4}{3}G \right) / \rho} \quad (5)$$

The equations of the constant cement model for porosity ϕ are as follows:

$$K_{dry} = \left(\frac{\phi/\phi_b}{K_b + 4G_b/3} + \frac{1-\phi/\phi_b}{K_s + 4G_b/3} \right) - 4G_b/3 \quad (6)$$

$$G_{dry} = \left(\frac{\phi/\phi_b}{G_b + z} + \frac{1-\phi/\phi_b}{G_s + z} \right)^{-1} - z, \quad z = \frac{G_b}{6} \frac{9K_b + 8G_b}{K_b + 2G_b} \quad (7)$$

where ϕ_b is porosity at which contact cement trend turns into constant cement trend (see Figure 10). Note that ϕ_b is smaller than critical porosity ϕ_c . Elastic moduli with subscript s are the moduli of the solid phase of the rock and elastic moduli with subscript b are the moduli of the rock at porosity ϕ_b . These moduli are calculated from the contact cementation theory (Dvorkin et al., 1994) with $\phi = \phi_b$. The relevant equations are in the appendix.

Table 4 summarizes the input parameters of the constant cement model used in the Stanford VI-E reservoir. 1% of calcite cement is assumed for the sand facies. Figure 10 compares the constant cement model (Avseth et al., 2000), the contact cement model (Dvorkin and Nur, 1996), and the Hashin-Shtrikman lower bound (Hashin and Shtrikman, 1963) for the brine-saturated channel in the Stanford VI-E.

Table 4. Parameters of the constant cement model

Parameter	Critical porosity, ϕ_c	Constant cement starting porosity, ϕ_b	Coordination number, n	Calcite Cement		
				P-wave modulus, M_c (GPa)	Shear modulus, G_c (GPa)	Poisson's ratio, ν_c
Value	0.38	0.37	9	120.9	32	0.32

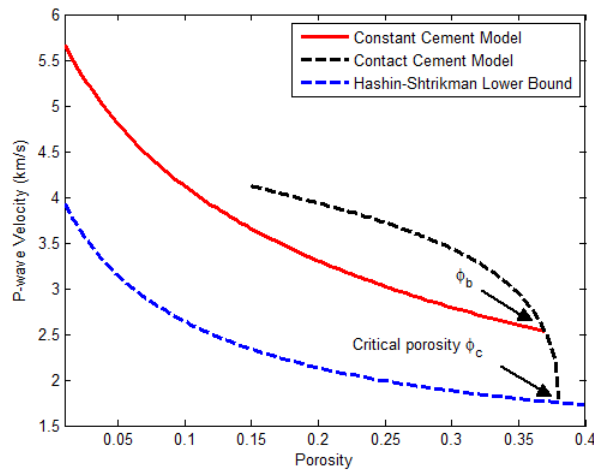


Figure 10. Constant cement model (Avseth et al., 2000), contact cement model (Dvorkin and Nur, 1996), and Hashin-Shtrikman lower bound (Hashin and Shtrikman, 1963) for brine-saturated channel facies.

The elastic modulus of the solid phase in the rock is obtained from the Voigt-Reuss-Hill average (Hill, 1952) of the mineral constituents (see Table 1 and 2). This is simply the arithmetic average of Voigt upper bound (Voigt, 1928) and the Reuss lower bound (Reuss, 1929):

$$M_{VRH} = \frac{M_V + M_R}{2} \quad (8)$$

where M_V is the Voigt upper bound of elastic modulus and M_R is the Reuss lower bound of elastic modulus as denoted by the following equations

$$M_V = \sum_{i=1}^N f_{m(i)} M_{m(i)}, \quad \frac{1}{M_R} = \sum_{i=1}^N \frac{f_{m(i)}}{M_{m(i)}}$$

$f_{m(i)}$ is the volume fraction of the mineral constituent i within the solid phase of the rock, and $M_{m(i)}$ is the elastic moduli of the mineral constituent i . Note that M can be any elastic modulus.

After having computed K_{dry} and G_{dry} using the constant cement model, Equation (9) and (10) are applied to obtain K_{sat} and G_{sat} for fluid-saturated condition of the sand facies in the Stanford VI-E reservoir.

$$K_{sat} = K_s \left[\frac{\phi K_{dry} - (1+\phi) K_f K_{dry} / (K_s + K_f)}{(1-\phi) K_f + \phi K_s - K_f K_{dry} / K_s} \right] \quad (9)$$

$$G_{sat} = G_{dry} \quad (10)$$

where the subscript s means the solid phase in the rock and f means the pore fluid. These equations correspond to one form of the Gassmann's fluid substitution (Gassmann, 1951) which is explained in the subsequent section.

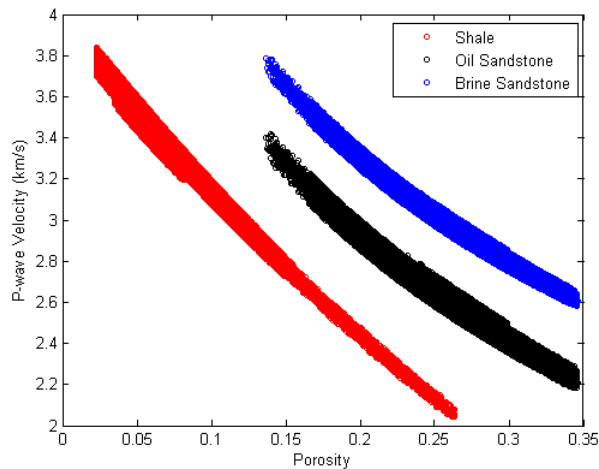


Figure 11. Porosity vs. P-wave velocity in the Stanford VI-E.

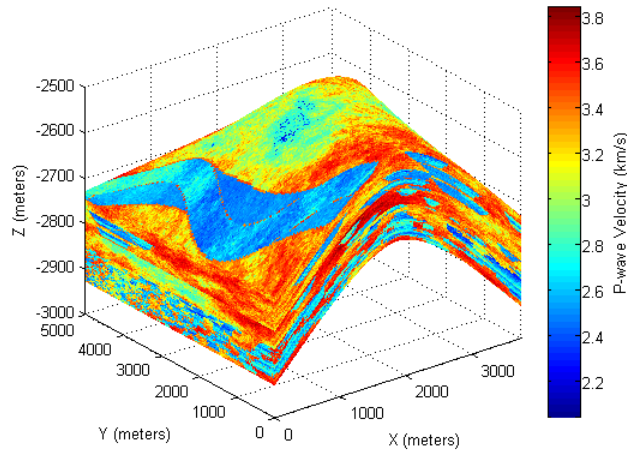


Figure 12. P-wave velocity model for the initial state of the Stanford VI-E.

For the shale facies in the Stanford VI-E reservoir, the power-law form of empirical relation between P-wave velocity and density suggested by Gardner et al. (1974) is used:

$$\rho = dV_p^f \quad (11)$$

where ρ is the bulk density of the rock in g/cc , V_p is the P-wave velocity of the rock in km/s , and the constants $d = 1.75$ and $f = 0.265$, which are typical values for shale (Castagna et al., 1993).

Figure 11 presents the crossplot between the porosity and P-wave velocity and Figure 12 shows the P-wave velocity model of the Stanford VI-E reservoir.

S-wave Velocity

For creating the S-wave velocities (V_s), the empirical relations between P-wave and S-wave velocities suggested by Castagna et al. (1985, 1993) are applied. Although the constant cement model provides S-wave velocities for the sand facies as well, those values are not used in the Stanford VI-E because empirical V_p - V_s relations from laboratory or log data are usually more reliable.

The famous mudrock line of Castagna et al. (1985) is used for the shale facies:

$$V_s = 0.862V_p - 1.172 \quad (km/s) \quad (12)$$

And the following relation of Castagna et al. (1993) for brine-saturated sandstone is used for the sand facies:

$$V_s = 0.804V_p - 0.856 \quad (\text{km/s}) \quad (13)$$

Note that the equation (11), (12) and (13) are for brine-saturated rocks, thus P-wave and S-wave velocities for brine-saturated condition are first computed and then the velocities for the initial saturation are obtained using the Gassmann's fluid substitution (Gassmann, 1951).

Figure 13 presents the crossplot between the porosity and S-wave velocity and Figure 14 shows the S-wave velocity model of the Stanford VI-E reservoir. The crossplot between P-wave and S-wave velocities is also shown in Figure 15.

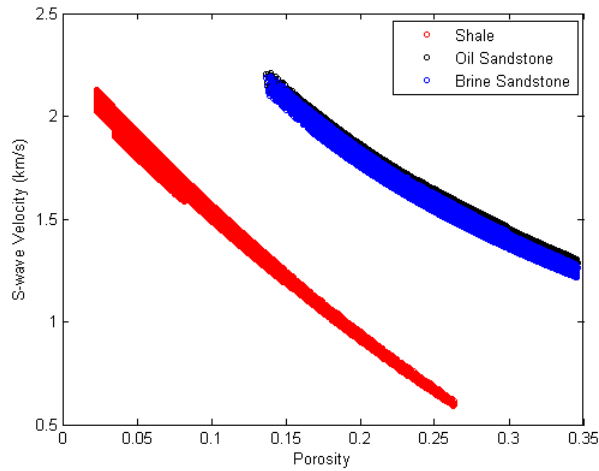


Figure 13. Porosity vs. S-wave velocity in the Stanford VI-E.

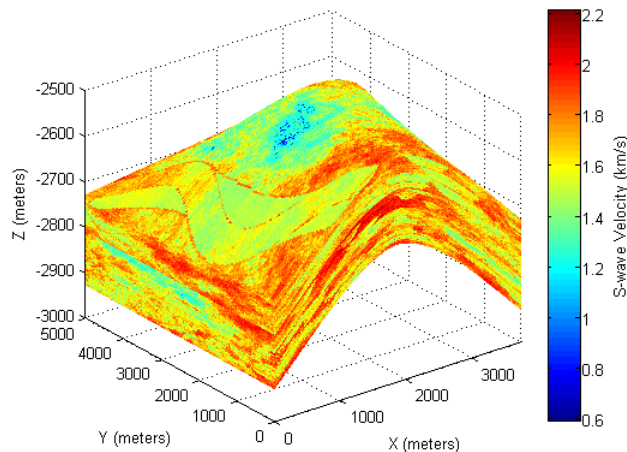


Figure 14. S-wave velocity model for the initial state of the Stanford VI-E.

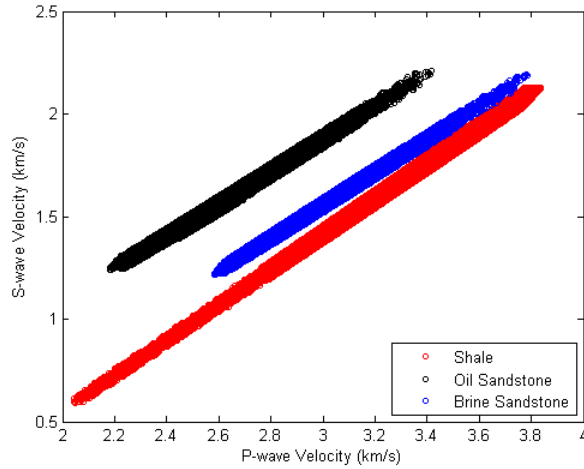


Figure 15. P-wave vs. S-wave velocity in the Stanford VI-E.

Fluid Substitution

Seismic velocities depend on pore fluid in rock because the elastic modulus and bulk density of the rock vary according to the pore fluid existing in it and the seismic velocities are functions of the elastic modulus and bulk density. Intuitively, a rock with less compressible fluid is stiffer than the same rock with more compressible fluid and, thus, it is more resistant to wave-induced deformation and its seismic velocities are faster.

In order to obtain the P-wave and S-wave velocities of oil-saturated rocks from those of brine-saturated rocks, the Gassmann's relation (Gassmann, 1951) is used in the Stanford VI-E reservoir. Gassmann's relation is a mathematical transformation which predicts how the elastic modulus of rock changes when one pore fluid in the rock is replaced with another pore fluid.

The procedure to obtain the seismic velocities of the rock saturated with fluid 2 from the velocities with fluid 1 by using Gassmann's fluid substitution is as follows. Firstly, the bulk and shear moduli of the rocks saturated with fluid 1 are computed from the density, P-wave and S-wave velocities:

$$K_{(1)} = \rho_{(1)} \left(V_{p(1)}^2 - \frac{4}{3} V_{s(1)}^2 \right) \quad (14)$$

$$G_{(1)} = \rho_{(1)} V_{s(1)}^2 \quad (15)$$

where $K_{(1)}$ and $G_{(1)}$ are the bulk and shear moduli, $\rho_{(1)}$ is the bulk density, and $V_{p(1)}$ and $V_{s(1)}$ are the P-wave and S-wave velocities of the rock saturated with fluid 1.

And then apply the Gassmann's relation to obtain the bulk and shear moduli of the rock saturated with fluid 2:

$$\frac{K_{(2)}}{K_s - K_{(2)}} - \frac{K_{f(2)}}{\phi(K_s - K_{f(2)})} = \frac{K_{(1)}}{K_s - K_{(1)}} - \frac{K_{f(1)}}{\phi(K_s - K_{f(1)})} \quad (16)$$

$$G_{(2)} = G_{(1)} \quad (17)$$

where $K_{(2)}$ and $G_{(2)}$ are the bulk and shear moduli of the rock saturated with fluid 2, K_s is the bulk modulus of the solid phase of the rock, $K_{f(1)}$ is the bulk modulus of fluid 1, $K_{f(2)}$ is the bulk modulus of fluid 2, and ϕ is porosity.

Compute the bulk density of the rock with fluid 2:

$$\rho_{(2)} = \rho_{(1)} + \phi(\rho_{f(2)} - \rho_{f(1)}) \quad (18)$$

where $\rho_{(2)}$ is the bulk density of the rock saturated with fluid 2, $\rho_{f(1)}$ is the density of fluid 1, and $\rho_{f(2)}$ is the density of fluid 2.

The P-wave and S-wave velocities of the rock saturated with fluid 2 are finally calculated as:

$$V_{p(2)} = \sqrt{\left(K_{(2)} + \frac{4}{3}G_{(2)} \right) / \rho_{(2)}} \quad (19)$$

$$V_{s(2)} = \sqrt{G_{(2)} / \rho_{(2)}} \quad (20)$$

where $V_{p(2)}$ and $V_{s(2)}$ are the P-wave and S-wave velocities of the rock saturated with fluid 2.

Gassmann's relation is based on the assumption that a monomineralic rock is changing from full saturation with one pure fluid to another pure fluid. Therefore, the bulk and shear moduli of the solid phase in the rock are obtained from the Voigt-Reuss-Hill average (Hill, 1952) of the mineral constituents as denoted by Equation (10).

As mentioned above, the effective fluid concept is used to model the state with two fluids. The bulk modulus of the effective fluid is calculated with the Reuss lower bound (or average), which describes an iso-stress situation. So it gives the exact modulus of uniformly mixed fluids at fine scales.

$$\frac{1}{K_f} = \sum_{i=1}^2 \frac{S_{f(i)}}{K_{f(i)}} \quad (21)$$

where K_f is the effective bulk modulus of the fluid mixture, $K_{f(i)}$ is the bulk modulus of the individual fluid i , and $S_{f(i)}$ denotes its saturation.

Random Variability

3% of uniform random variability for the bulk modulus of the shale facies and 5% for the bulk modulus of the sand facies are added for the initial saturation of the Stanford VI-E reservoir. 5% of uniform random variability is incorporated into the shear modulus of shale and sand facies. And then the P-wave (Figure 11) and S-wave velocities (Figure 13) for the initial state are computed with the density with random variability (Figure 8).

As a reference data set, we want to create the Stanford VI-E reservoir as error-free data with natural variability. So users can test algorithms with the data without errors, or add any amount and distribution of errors to the data and then test algorithms for their own purposes. In order to do that, the data with random variability for the initial state are kept for creating time-lapse (4D) data so they can be reversible with fluid substitution. This is an important aspect in creating 4D seismic data without errors because errors are inevitable if calculating the seismic data at different times during production and adding random variability to the 4D seismic data for each time step separately.

The Hashin-Shtrikman bounds (Hashin and Shtrikman, 1963) give the narrowest range of elastic moduli in which an isotropic linear elastic composite can exist. If the synthetic moduli with random variability violate the Hashin-Shtrikman bounds, the values corresponding to different fluid saturations obtained by the Gassmann's relation tend to be non-physical (complex-valued), thus 4D seismic data cannot be computed.

Adding randomness to the elastic moduli, it is much easier to be within the Hashin-Shtrickman bounds than adding randomness to the seismic velocities because the Hashin-Shtrickman bounds are bounds for elastic moduli. The independent variability of the P-wave and S-wave velocities can cause the larger amount of randomness in bulk modulus (see Equation (16)) that can easily violate the bounds, specially the lower bound for smaller porosities.

Elastic Attributes

Elastic attributes derived from seismic data can provide more accurate and sensitive indicators to the structural, stratigraphic, lithological and fluid features of a reservoir than traditional seismic images in reservoir characterization. Among various attributes that have been

computed and used from seismic data, the following is a list of elastic attributes contained in the Stanford VI-E reservoir: acoustic impedance, S-wave impedance, elastic impedance, Lame's parameters, and Poisson's ratio.

In the Stanford VI-E, those values are calculated from mathematical expressions of the density, P-wave and S-wave velocities based on elasticity theory. These attributes are, therefore, represented at the point scale (geostatistical scale). In real reservoir characterization, seismic inversion is performed to transform seismic data to these elastic attributes so we can only obtain the seismic scale attributes. Nonetheless, we do not perform any explicit inversion or any filtering and smoothing to create the seismic scale data. This can give flexibility in choosing forward modeling methods or using a small part of the reservoir.

Acoustic Impedance and S-wave Impedance

The impedance of an elastic medium is the ratio of the stress to the particle velocity (Aki and Richards, 1980) and is given by the product of density and wave propagation velocity.

Acoustic impedance or P-wave impedance (AI) is the product between density and P-wave velocity:

$$AI = \rho V_p \quad (22)$$

And S-wave impedance (SI) is the product of density and S-wave velocity:

$$SI = \rho V_s \quad (23)$$

Elastic Impedance

Elastic impedance (EI) is a pseudo-impedance attribute for non-zero incidence angles (Connolly, 1999; Mukerji et al., 1998). This pseudo-impedance is the far-offset equivalent of the conventional zero-offset or near-offset acoustic impedance. Since the far-offset stacks depend not only on P-wave velocity and density but also on S-wave velocity, the elastic impedance carries information about V_p/V_s ratio.

Mukerji et al. (1998) defined the elastic impedance in terms of the elastic P-P reflection coefficient at an incidence angle θ :

$$EI(\theta) = e^{2\int R(\theta)dt} \quad (24)$$

where $R(\theta)$ is the elastic P-P reflection coefficient at θ . The exact expression for $R(\theta)$ is

described by the Knott-Zoeppritz equation (Knott, 1899; Zoeppritz, 1919). However, various authors have presented approximations to this equation due to its complexity (e.g., Bortfeld, 1961; Shuey, 1985). By using one of the approximations by Aki and Richards (1980), Mukerji et al. (1998) provided the following expression for the elastic impedance:

$$EI(\theta) = V_p^{1+\tan^2 \theta} V_s^{-\frac{8}{\rho} \left(\frac{V_s}{V_p} \right)^2 \sin^2 \theta} \quad (25)$$

As expected, the elastic impedance is a function of P-wave velocity, S-wave velocity, density and incidence angle θ . This attribute is typically obtained by inversion of far-offset stacks. Accordingly, the elastic impedance in the Stanford VI-E reservoir is calculated for $\theta = 30^\circ$.

Lame's Parameters λ and μ

Lame's parameters λ and μ have also been used as seismic attributes to discriminate lithology and detect hydrocarbon (e.g., Goodway et al., 1997; Gray et al., 1999). These parameters are fundamental elastic constants in linear elasticity theory and can be directly related to seismic velocities and density as follows. The second Lame's parameter μ is the same with shear modulus G :

$$\lambda = \rho(V_p^2 - 2V_s^2) \quad (26)$$

$$\mu = \rho V_s^2 \quad (27)$$

Poisson's Ratio

As an indicator of fluid type, Poisson's ratio ν can be obtained by pre-stack inversion of multi-offset data (Avseth et al., 2005). It can be expressed in terms of seismic velocities as follows:

$$\nu = \frac{V_p^2 - 2V_s^2}{2(V_p^2 - V_s^2)} \quad (28)$$

Figure 16 provides the models of the elastic attributes for the initial state of the Stanford VI-E reservoir. Some crossplots are also presented in Figure 17 to show how they discriminate fluids and lithology.

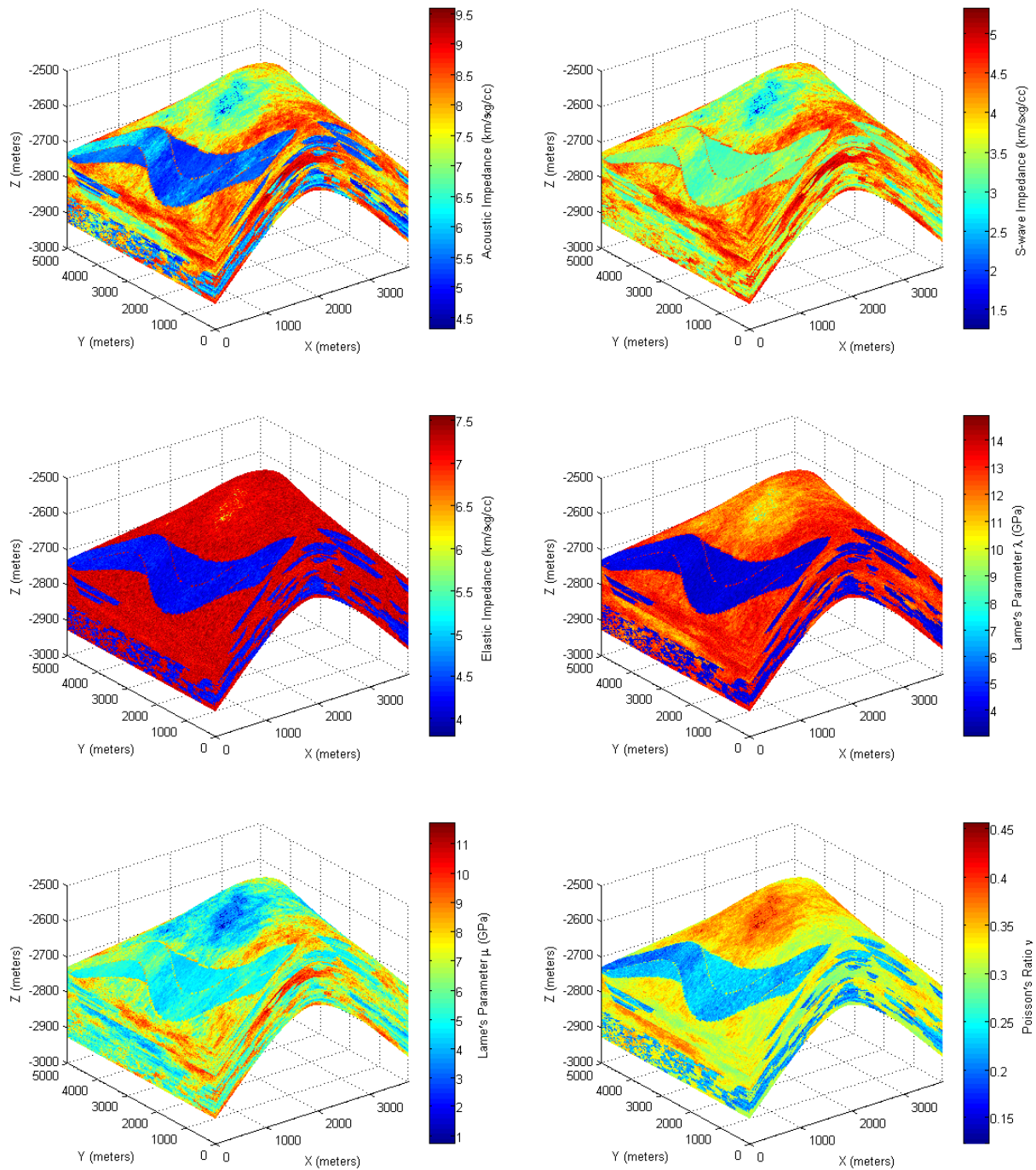


Figure 16. Elastic attribute models for the initial state of the Stanford VI-E: acoustic impedance (top-left), S-wave impedance (top-right), elastic impedance (middle-left), Lame's parameter λ (middle-right), Lame's parameter μ (bottom-left), and Poisson's ratio (bottom-right).

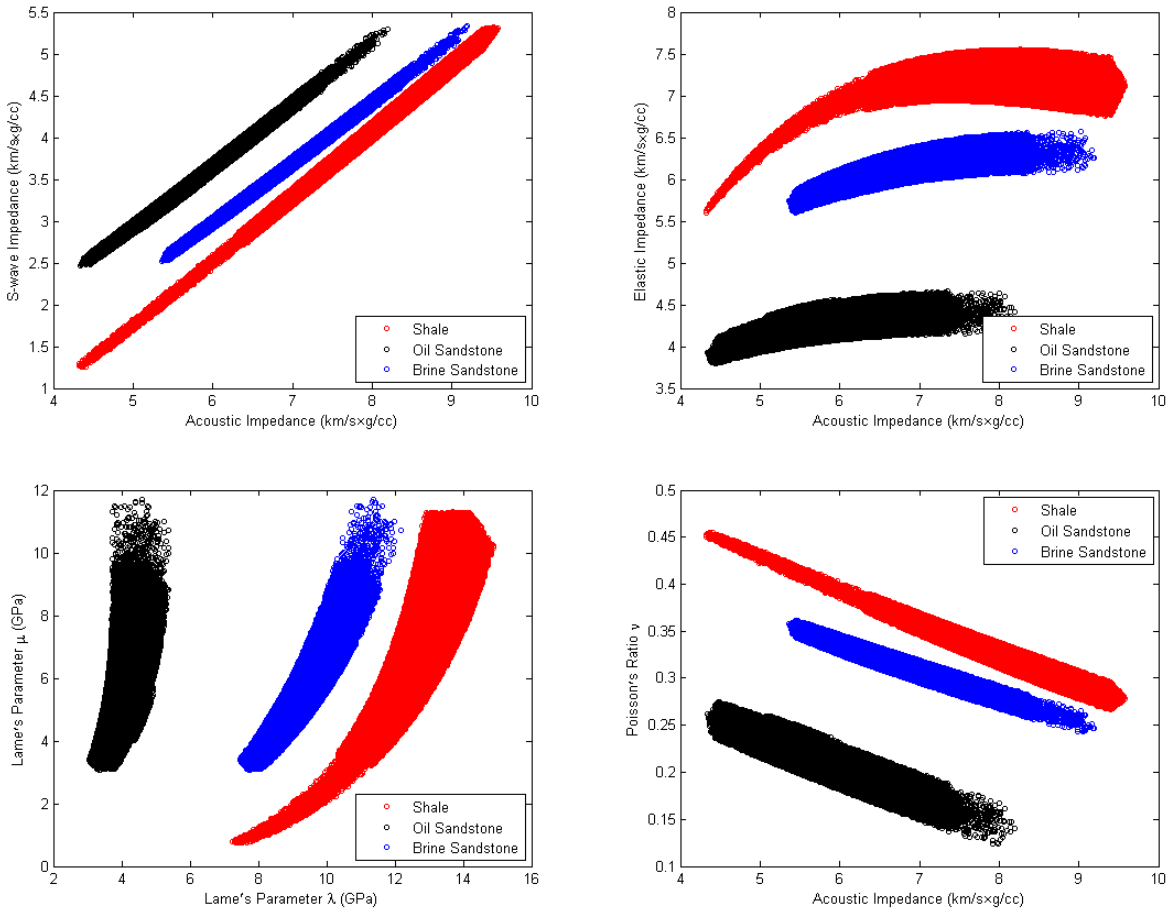


Figure 17. Crossplots between elastic attributes in the Stanford VI-E.

Electrical Resistivity

The electrical resistivity of rock formations is one of the basic petrophysical logs to estimate lithology and fluid saturation in reservoirs. It indicates how strongly the formations resist the electric current. Electrical conductivity is the reciprocal quantity of the electrical resistivity, which measures the ability to conduct the electric current.

Recently, some electromagnetic imaging techniques have been applied in reservoir monitoring, for example, cross-well electromagnetic methods (Alumbaugh et al., 1993; Wilt et al., 1995) or controlled-source electromagnetic methods (CSEM) (Constable and Cox, 1996; MacGregor et al., 2001). Since electrical resistivity strongly depends on pore fluids, the electromagnetic methods, which estimate the distribution of electrical resistivity in reservoirs, can be very useful to specify fluid saturation and hydrocarbon-filled zones.

In the Stanford VI-E reservoir, the electrical resistivity is newly created based on the well known empirical relationships (Archie, 1942; Waxman and Smits, 1968) in order to study reservoir management algorithms using time-lapse electromagnetic and seismic data.

Sandstone

Most crustal rocks are made up of minerals that are semiconductors or insulators (silicates and oxides). Conducting electric currents in fluid-saturated rocks caused by an applied DC voltage arise primarily from the flow of ions within the pore fluids (Mavko et al., 2009). Therefore, many studies have attempted to develop empirical relationships between porosity, electrical resistivity of pore fluid, saturation, and electrical resistivity of rocks.

Archie (1942) published an empirical relation for brine-saturated clean sandstones, which is still the most widely used in interpreting resistivity logs. This method, sometimes referred to as the Archie's law, is used to generate the electrical resistivity for the sand facies in the Stanford VI-E.

Formation factor F is defined as the ratio of the bulk resistivity of the fully saturated rock to the resistivity of the pore fluid:

$$F = \frac{R_0}{R_w} = \frac{\sigma_w}{\sigma_0} \quad (29)$$

where R_0 and σ_0 are the electrical resistivity and conductivity of the rock fully saturated with the pore fluid and R_w and σ_w are the electrical resistivity and conductivity of the pore fluid.

Archie's first law relates the formation factor to the porosity of fully brine-saturated sandstones as follows:

$$F = a\phi^{-m} \quad (30)$$

where ϕ is the porosity of the rock, a is the tortuosity constant, and m is the cementation exponent. By combining Equation (29) and (30), the electrical resistivity of fully brine-saturated sandstones is given by:

$$R_0 = a\phi^{-m} R_w \quad (31)$$

For partially brine-saturated sandstones, Archie's second law provides the relationship between brine saturation and electrical resistivity:

$$S_w^{-n} = \frac{R_t}{R_0} \quad (32)$$

where S_w is the saturation of brine, n is the saturation exponent, R_t is the electrical resistivity of the partially saturated rock at the brine saturation S_w , and R_0 is the electrical resistivity of the same rock that is fully saturated with brine. Therefore, the resulting equation for obtaining the resistivity of the sand facies in the Stanford VI-E is:

$$R_t = a S_w^{-n} \phi^{-m} R_w \quad (33)$$

Table 5 summarizes the parameters used in the Stanford VI-E reservoir. Typical values are assumed for the parameters a , n , and m . The electrical resistivity of brine is estimated based on the salinity (20,000 NaCl ppm) of the Stanford VI-E. Keller (1987) gives an excellent summary of typical parameters of the Archie's law and electrical resistivity of minerals and fluids.

Shale

Unlike silicates and oxides, clay minerals offer additional conductivity through a diffuse double layer which forms around clay particles. The thickness of the double layer depends on the salinity i.e. brine conductivity (resistivity). Hence, this contribution of clay minerals should be considered in estimating the electrical resistivity of shaly-sands and shale. Numerous formulations have been developed to model the electrical resistivity of shaly-sands (e.g., Simandoux, 1963; Waxman and Smits, 1968; Poupon and Leveaux, 1971; Clavier et al., 1984) and almost all of them modify the Archie's model and incorporate the additional conductivity introduced by clay minerals into it.

Of these models, the Waxman-Smits model (Waxman and Smits, 1968) is used to generate the electrical resistivity for the shale facies in the Stanford VI-E. For fully brine-saturated shales, the equation of Waxman-Smits model is given by:

$$\sigma_0 = \frac{1}{F} (\sigma_w + B Q_v) \quad (34)$$

where σ_0 are the electrical conductivity of the shale that is fully saturated with brine, F is the formation factor denoted by Equation (32), σ_w are the electrical conductivity of brine, B is the equivalent conductance of sodium clay exchange cations, and Q_v is the cation exchange capacity per unit pore volume. B and Q_v are obtained by the following equations:

$$B = 4.6(1 - 0.6e^{-\sigma_w/1.3}), \quad Q_v = \frac{CEC(1-\phi)\rho_s}{\phi}$$

where CEC is the cation exchange capacity, ϕ is the porosity, ρ_s is the density of the solid phase in shale.

For partially brine-saturated shales, the Waxman-Smits model provides the following equation:

$$\sigma_t = \frac{\sigma_w S_w^n}{F} + \frac{BQ_v S_w^{n-1}}{F} \quad (35)$$

where σ_t is the electrical conductivity of the partially saturated shale at the brine saturation S_w . Therefore, the resulting equation for obtaining the resistivity of the shale facies in the Stanford VI-E is:

$$R_t = \frac{1}{\sigma_t} = 1 \left/ \left(\frac{\sigma_w S_w^n}{a\phi^{-m}} + \frac{BQ_v S_w^{n-1}}{a\phi^{-m}} \right) \right. \quad (36)$$

The same values with the sand facies are assumed for the parameters a , n , and m (Table 5).

In order to compute Q_v , the cation exchange capacity (CEC) is estimated based on the assumption that illite is the clay mineral in the Stanford VI-E. Carroll (1959) reported 10-40 $meq./100g$ as the CEC of illite and we assume that our illite has the CEC of $30meq./100g$. By combining with the mineral fractions and densities (see Table 1 and 2), the CEC of the shale facies is obtained by the following equation:

$$CEC(facies) = \frac{\sum_{i=1}^N f_{m(i)} \rho_{m(i)}}{\sum_{i=1}^N f_{clay} \rho_{clay}} CEC(illite) \quad (37)$$

Table 5. Parameters of the Archie's and Waxman-Smits models

Parameter	Tortuosity constant, a	Cementation exponent, m	Saturation exponent, n	Brine resistivity, $R_w (\Omega \cdot m)$	$CEC (meq./g)$	
					Floodplain	Boundary
Value	1.0	1.8	2.0	0.25	0.253	0.268

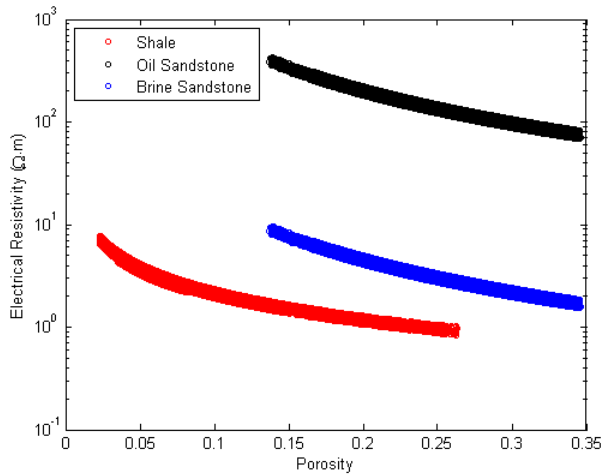


Figure 18. Porosity vs. electrical resistivity in the Stanford VI-E.

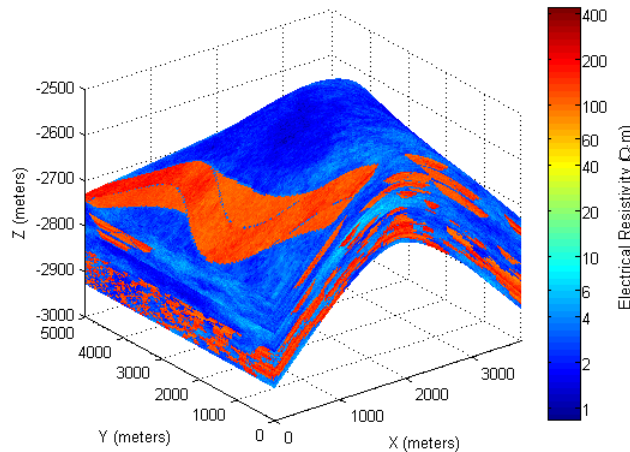


Figure 19. Electrical resistivity model for the initial state of the Stanford VI-E.

Figure 18 presents the crossplot between the porosity and electrical resistivity and Figure 19 shows the electrical resistivity model of the Stanford VI-E reservoir. 10% of random variability is added to the simulated electrical resistivity.

Reservoir Flow Simulation

Reservoir flow simulation is an important tool for predicting fluid flow, forecasting hydrocarbon production, and developing the optimal recovery plans in reservoir management. It is a numerical simulation solving the flow equations in porous medium using two basic petrophysical properties; porosity and permeability, and fluid properties.

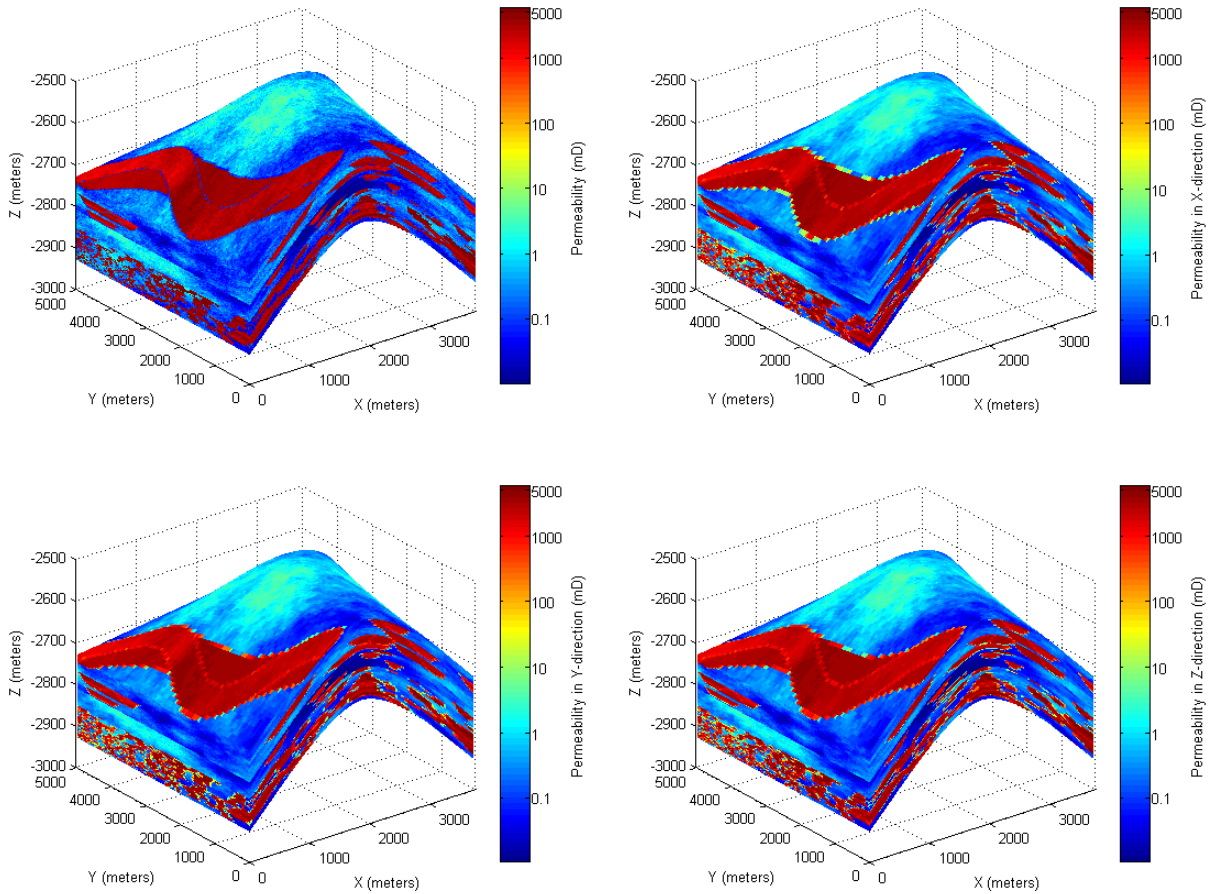


Figure 20. Original scale and upscaled effective permeability; original scale κ (top-left), effective κ_x (top-right), effective κ_y (bottom-left), and effective κ_z (bottom-right).

From the simulated porosity and permeability in the Stanford VI-E, the reservoir flow simulation is performed to obtain the production data, which can be potentially used for history matching algorithms and the fluid saturation changes to create time-lapse electromagnetic and seismic data.

Upscaling of Reservoir Model

The Stanford VI-E reservoir consists of 6,000,000 cells ($150 \times 200 \times 200$), which are usually not feasible in conventional flow simulators with typical computing power. Hence, upscaling of the reservoir properties is necessary to reduce the size of the reservoir to the manageable level in terms of flow simulation.

The same upscaling technique used in the Stanford VI, which is referred to as the flow-based upscaling technique, is applied in the Stanford VI-E reservoir. This technique produces effective

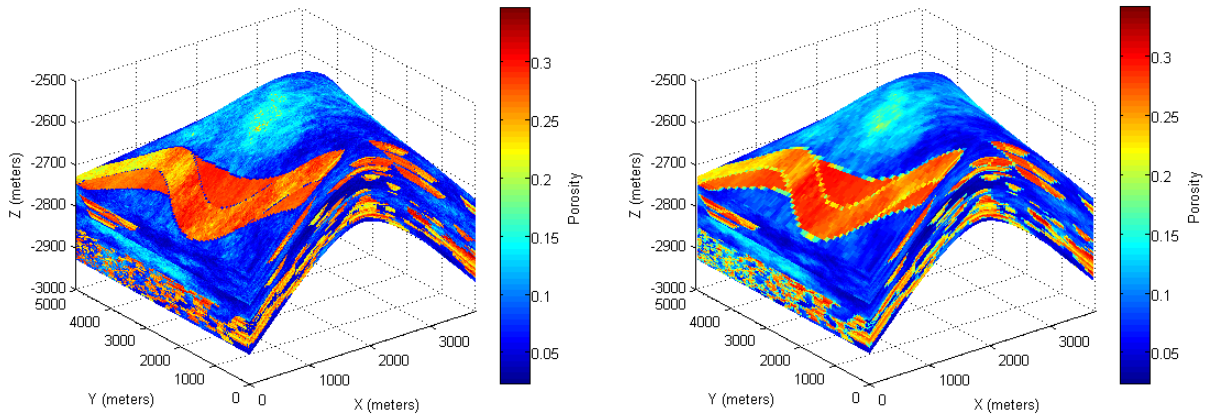


Figure 21. Original scale (left) and upscaled porosity (right). (Modified from Castro et al., 2005)

permeability to replicate the fine scale behavior in overall flow rate by using a single-phase pressure solver, **FLOWSIM** (Deutsch, 1989). When upscaling isotropic permeability, the resulting effective permeability becomes anisotropic, so three effective permeabilities in each direction x , y , and z are obtained for the upscaled reservoir. Figure 20 shows the resulting effective permeability κ_x , κ_y , and κ_z with the original scale permeability.

Porosity is upscaled simply using a linear block average. Since the porosity of the Stanford VI is used in the Stanford VI-E, the upscaled porosity is also the same (Figure 21).

Flow Simulation

The flow simulation is performed using the commercial software **ECLIPSE**. A fully-implicit and three-dimensional black oil simulator is used. In the Stanford VI-E, there exist only two phases; brine and oil, and we inject brine at a certain time during oil production. Table 6 summarizes the density and PVT properties of brine and oil. Figure 22 shows the relative permeability used in the flow simulation. No capillary pressure is considered ($P_c = 0$).

Table 6. Brine and oil density and PVT properties in flow simulation

Fluid \ Property	Density (lb/ft^3)	PVT properties		
		Pressure ($psia$)	Viscosity (cP)	Formation volume factor
Brine	61.80	14.7	0.325	1.0
Oil	45.09	14.7	1.16	1.012
		10,000	1.2	0.95

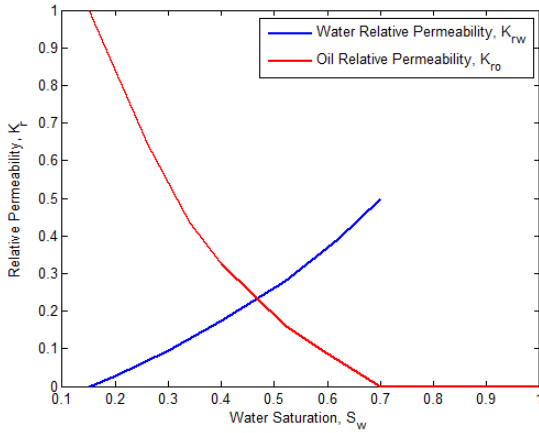


Figure 22. Brine and oil relative permeability curves (Castro et al., 2005).

In the Stanford VI, the flow simulation was conducted for the situation that the entire reservoir is oil saturated regardless of facies; with the water-oil contact at 9,840 ft (3,000 m) depth. This is an unusual case in real reservoirs. With the relatively high permeability of the shale facies of the Stanford VI, the hydrocarbon flow is unrealistically uniform and the time-lapse data are not quite useful for testing reservoir monitoring algorithms.

Therefore, as the initial state of the Stanford VI-E reservoir, it is assumed that all the sand facies (*point bar* and *channel*) are oil saturated (residual brine saturation condition; $S_{brine} = 0.15$ and $S_{oil} = 0.85$) while all the shale facies (*floodplain* and *boundary*) are fully brine saturated ($S_{brine} = 1$). And, as described before, the shale permeability is reduced by the factor of 100 in the Stanford VI-E reservoir.

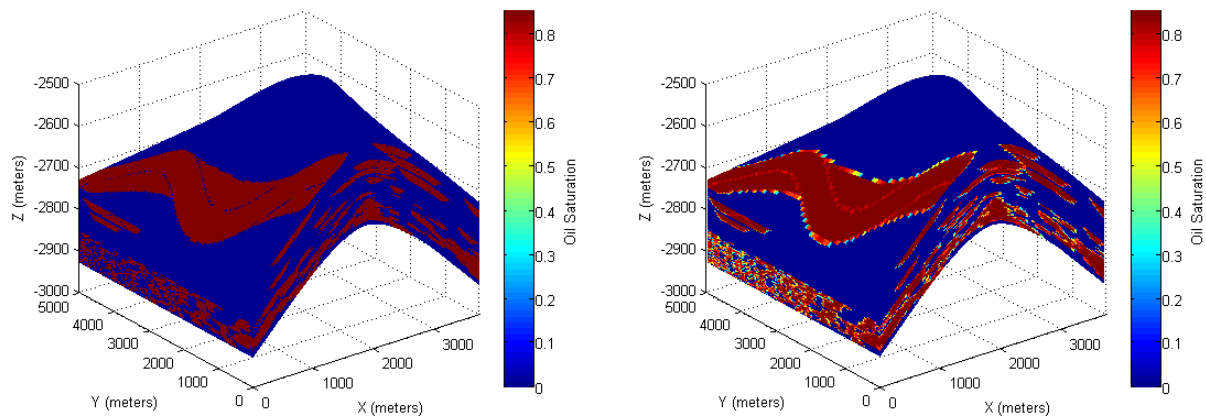


Figure 23. Original scale (left) and upscaled initial oil saturation.

In order to lead the fluid flow to occur mostly through the sand facies, the net to gross value (NTG) of pore volume is also introduced in the flow simulation. This means that only a part of the pore volume ($NTG \times \phi$) contributes to the flow. NTG of 0.05 and 1 are assigned to the shale facies and the sand facies respectively in the Stanford VI-E. Therefore only 5% of shale volume can bear oil during production.

The initial saturation and net to gross values also need to be upscaled to the size of flow simulation. Since both variables are volumetric ratios, they are upscaled as porosity-weighted block averages as denoted by Equation (38) and (39):

$$S_{brine(u)} = \frac{\sum_i^N \phi_{(i)} S_{brine(i)}}{\sum_i^N \phi_{(i)}} \quad (38)$$

$$NTG_{(u)} = \frac{\sum_i^N \phi_{(i)} NTG_{(i)}}{\sum_i^N \phi_{(i)}} \quad (39)$$

where $S_{brine(u)}$ is the upscaled brine saturation, $S_{brine(i)}$ is the brine saturation of the point scale cell i which is united as one cell in flow simulation, $\phi_{(i)}$ is the porosity of cell i , $NTG_{(u)}$ is the upscaled net to gross, $NTG_{(i)}$ is the net to gross of cell i , and N is the number of the point scale cells which are represented as one cell after upscaling; In this case $N = 8$. Figure 23 and 24 present the upscaled initial oil saturation and net to gross with the original scale values.

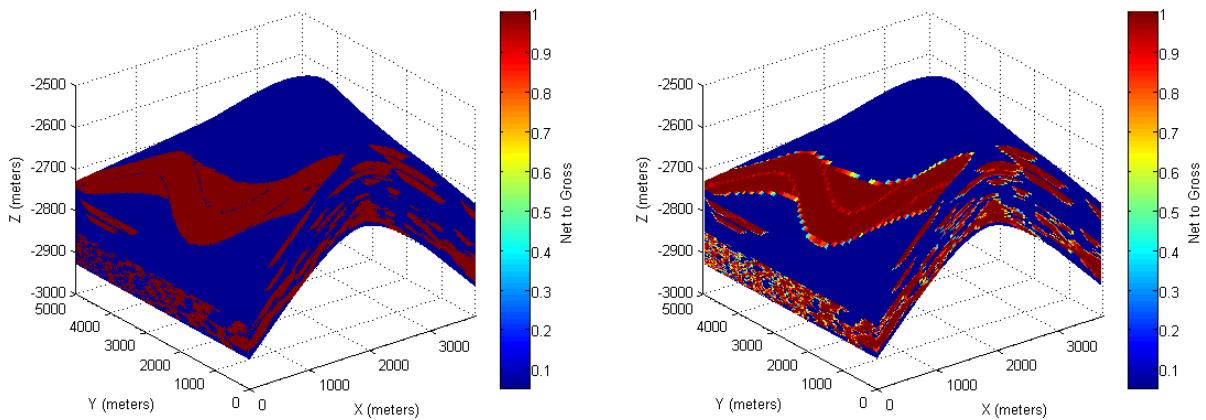


Figure 24. Original scale (left) and upscaled net to gross values (right).

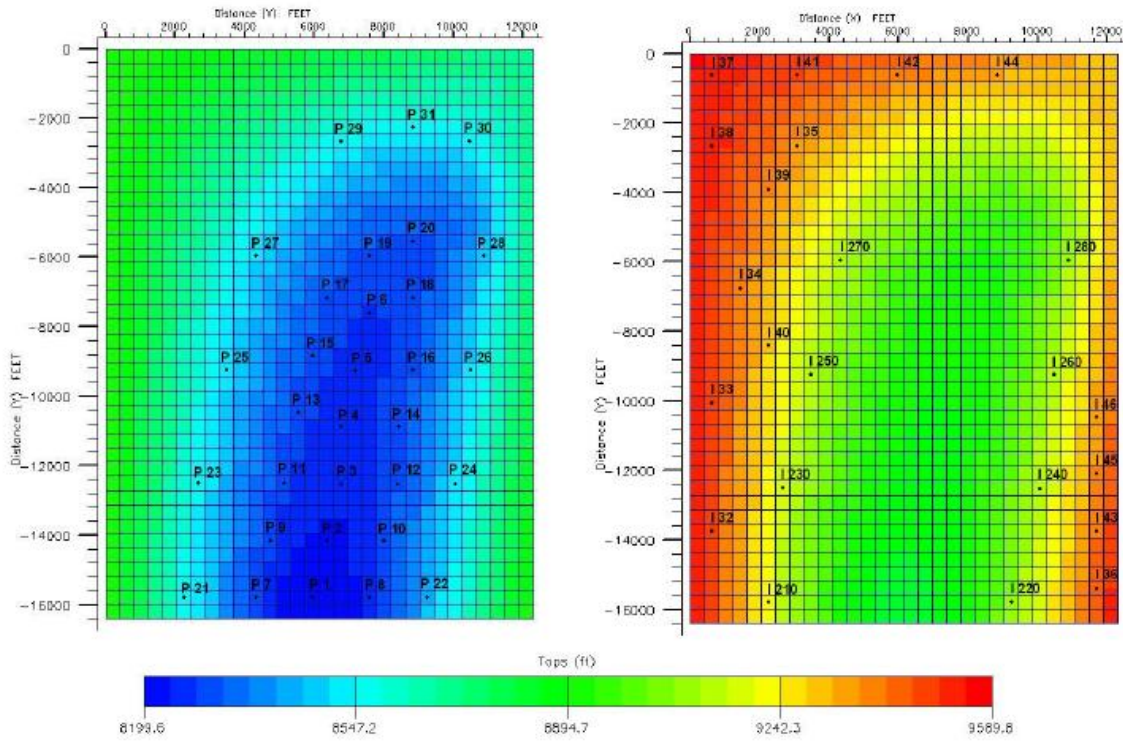


Figure 25. Location maps of production wells (left) and injection wells (right). The color represents the top depth of wells (ft). (Castro et al., 2005)

Except for the permeability, initial saturation, and net to gross explained above, the other conditions for the flow simulation are the same with the Stanford VI reservoir. An active constant flux aquifer exists below the reservoir and its water inflow rate is 31,000 STB/day. The flow simulation starts with 6 production wells in January, 1975 (primary production). And the production continues for 30 years with 31 oil production wells and 15 water injection wells. The location map of the injectors and producers is shown in Figure 25.

A summary of the production schedule is given in Table 7. Not all wells start producing oil or injecting water at the same time, as is typical of an actual reservoir development where new wells are constantly added. Production wells are controlled by constant liquid production rate with a bottomhole pressure (BHP) constraint of 2,700 psia, while injector wells are controlled by constant water injection rate. For the producer P21 through P28, an economic limit is set such that they are converted to water injectors after they reach the water cut higher than 0.5.

Figure 26 shows the oil saturation at different times (5, 15, and 30 years after production) during production obtained by the flow simulation result.

Table 7. Summary of the production schedule (Modified from Castro et al., 2005)

Data	Operation
Jan. 1975	Start primary oil production with P1 to P6.
Jan. 1979	P22 and P24 are open to production.
Jan. 1981	P26, P28, and P30 are open to production.
Jan. 1983	P21, P23, P25, P27, P29, and P31 are open to production.
Jan. 1986	P7, P9, P11, P13, P15, P17, and P19 are open to production. Start water injection with I32, I33, I34, I36, I37, I38, I41, I43, and I45.
Jan. 1989	P8, P10, P12, P14, P16, P18, and P20 are open to production. I35, I39, I40, and I42 are open to injection.
Oct. 1989	I44 and I46 are open to injection.
Jan. 1995	Increase production rate of P1 to P6. Increase injection rate of I36, I42, I43, I44, I45, and I46.
Jan. 1998	Increase production rate of P7 to P20.
Jan. 2001	Increase production rate of P1 to P6.
Mar. 2003	Increase production rate of P8, P10, P12, P14, P16, P18 and P20.
Mar. 2005	End of the flow simulation

Time-lapse Data

Time-lapse data are simply several data sets at different times over the same area to examine changes in subsurface during reservoir development. In order to generate the time-lapse seismic and electromagnetic data in the Stanford VI-E, the same procedures described before are applied based on the change in saturation obtained from the flow simulation.

Downscaling of Saturation

Before calculating the petrophysical properties, we first downscale fluid saturation at the flow simulation scale (coarse scale) to the geostatistical scale (fine scale). Since the net to gross values are introduced in the flow simulation, the following procedure is applied.

Suppose that $S_{brine(u,NTG)}$ is defined as the brine saturation only in active pore volume ($NTG \times \phi$):

$$S_{\text{brine}(u,NTG)} = \frac{\text{Brine volume within active pore volume}}{\text{Active pore volume} = NTG_{(u)} \phi_{(u)} V} \quad (40)$$

where $S_{\text{brine}(u,NTG)}$ is the brine saturation only considered in active pore volume of a coarse scale cell, $NTG_{(u)}$ is the upscaled net to gross, $\phi_{(u)}$ is the upscaled porosity, and V is the total volume of a coarse cell.

By assuming that the fluid in inactive pore volume is 100% brine (only shale facies has inactive pore volume in the Stanford VI-E), the brine saturation can be described as follows:

$$S_{\text{brine}(u)} = S_{\text{brine}(u,NTG)} NTG_{(u)} + (1 - NTG_{(u)}) \quad (41)$$

where $S_{\text{brine}(u)}$ is the brine saturation of a coarse cell. Thus, $S_{\text{brine}(u,NTG)}$ is expressed as:

$$S_{\text{brine}(u,NTG)} = \frac{S_{\text{brine}(u)} - (1 - NTG_{(u)})}{NTG_{(u)}} \quad (42)$$

If we assume the brine saturation in active pore volume is the same for all the fine scale cells represented by one coarse cell, $S_{\text{brine}(u,NTG)}$ is constant in those fine scale cells. Therefore, the brine saturation of a fine scale cell is given by:

$$S_{\text{brine}(i)} = S_{\text{brine}(u,NTG)} NTG_{(i)} + (1 - NTG_{(i)}) \quad (43)$$

where $S_{\text{brine}(i)}$ is the brine saturation of a fine scale cell i , and $NTG_{(i)}$ is the net to gross of a fine scale cell i .

In combination with Equation (42), the brine saturation at fine scale is computed from the brine saturation at coarse scale as follows:

$$S_{\text{brine}(i)} = \frac{S_{\text{brine}(u)} - (1 - NTG_{(u)})}{NTG_{(u)}} NTG_{(i)} + (1 - NTG_{(i)}) \quad (44)$$

Note that the **ECLIPSE** directly gives $S_{\text{brine}(u,NTG)}$ as saturation.

Figure 26 shows the oil saturation at 5, 15, and 30 years after production obtained by the flow simulation result and the downscaled saturation.

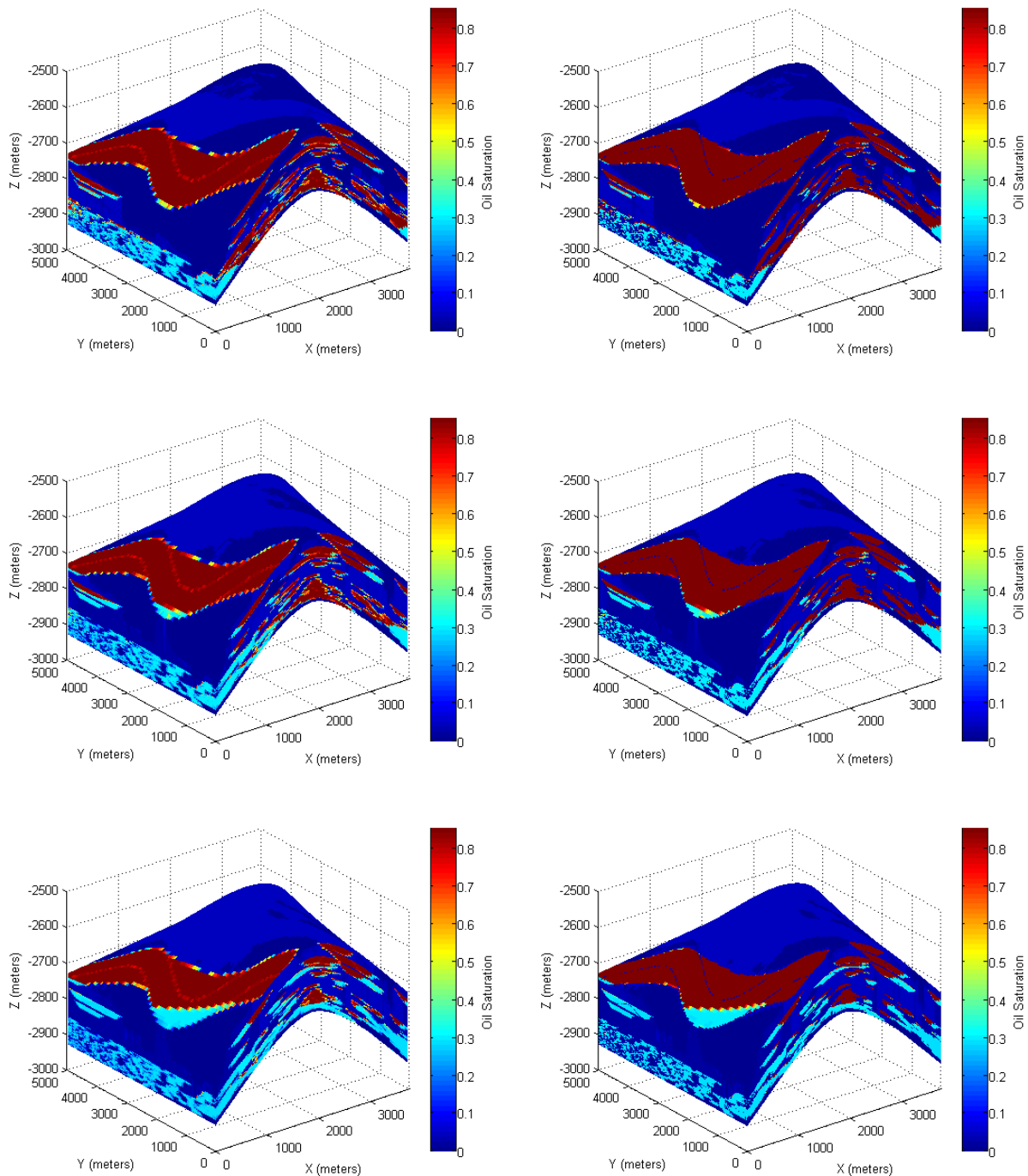


Figure 26. Oil saturation at 5 (top), 15 (middle), and 30 (bottom) years after production obtained from flow simulation (left) and the downscaled saturation (right).

Petrophysical Properties

The density, P-wave and S-wave velocities are computed using the Gassmann's fluid substitution (see Equation (16) to (22)) at different times (1-30 years after production) for the Stanford VI-E reservoir. Figure 27, 28, and 29 show the petrophysical properties at initial state and 5, 15, and 30 years after production based on the downscaled saturation.

As mentioned earlier, the Stanford VI-E reservoir is designed as an error-free data set with natural variability. So the density, P-wave and S-wave velocities with random variability for the initial state are used to calculate the time-lapse petrophysical properties.

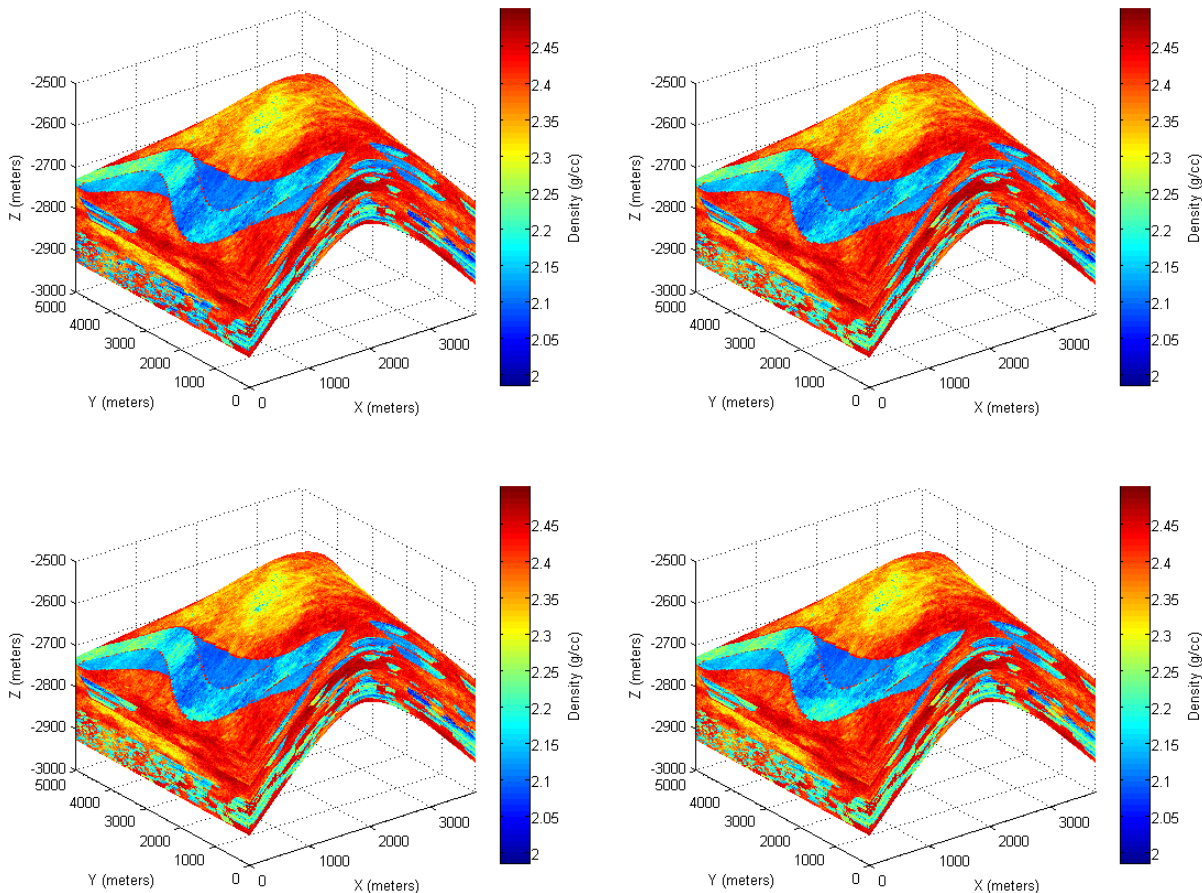


Figure 27. Density at the initial state (top-left) and 5 (top-right), 15 (bottom-left), and 30 (bottom-right) years after production. Color scales are matched.

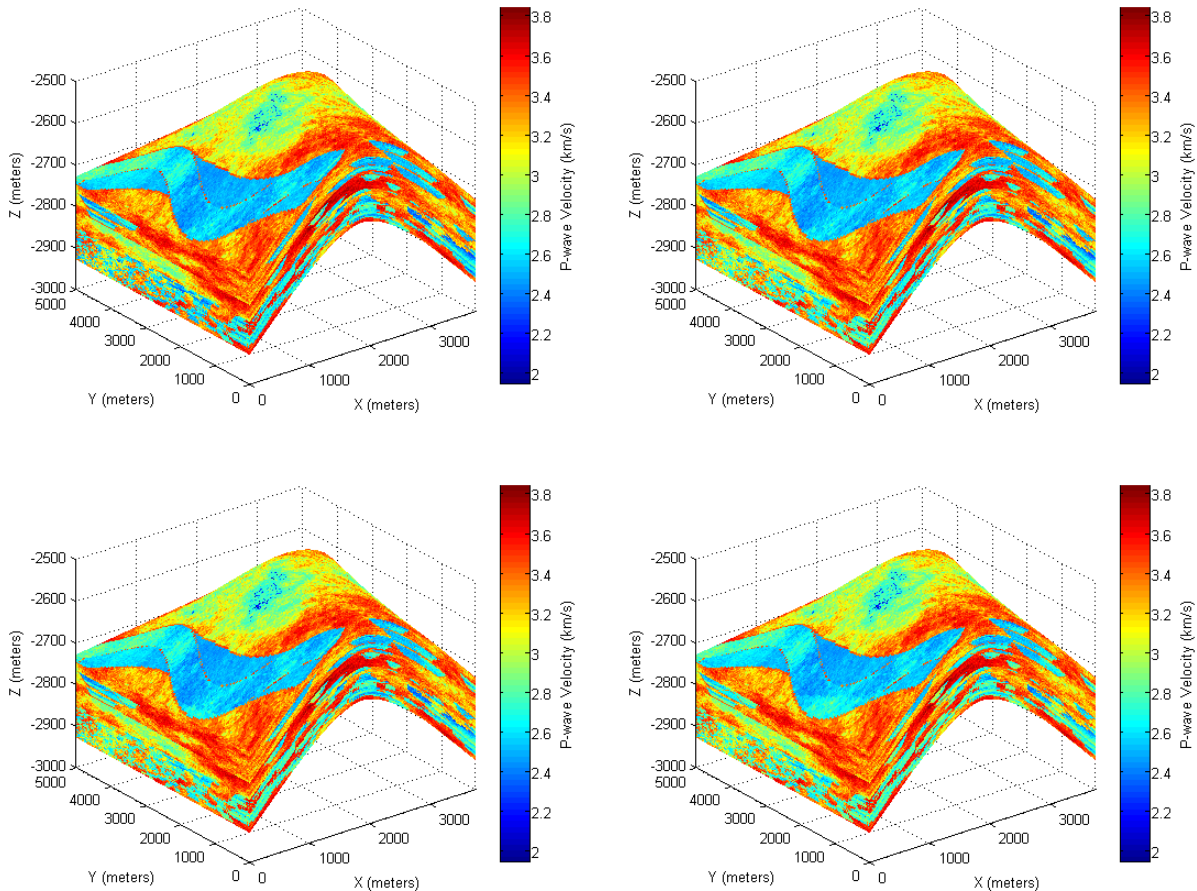


Figure 28. P-wave velocity at the initial state (top-left) and 5 (top-right), 15 (bottom-left), and 30 (bottom-right) years after production. Color scales are matched.

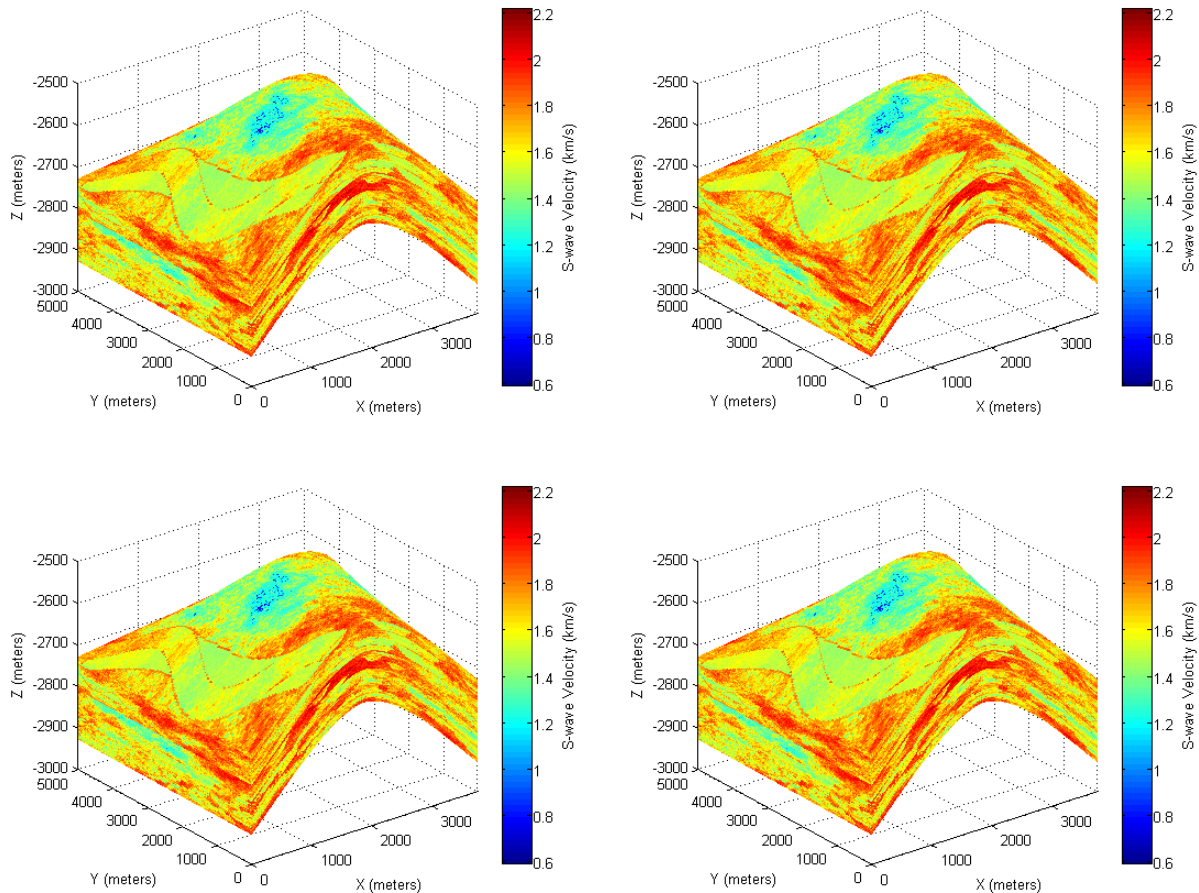


Figure 29. S-wave velocity at the initial state (top-left) and 5 (top-right), 15 (bottom-left), and 30 (bottom-right) years after production. Color scales are matched.

Elastic Attributes

Elastic attributes are also computed using the density, P-wave and S-wave velocities at different times. Figure 30, 31, and 32 present the acoustic impedance, S-wave impedance, and elastic impedance at initial state and 5, 15, and 30 years after production. Figure 33 and 34 show the Lame's parameters. And Figure 35 presents the Poisson's ratio. From those figures, we can see that the attributes mainly related to S-wave velocity; S-wave impedance, Lame's parameter μ (shear modulus) are not much sensitive to the change in saturation.

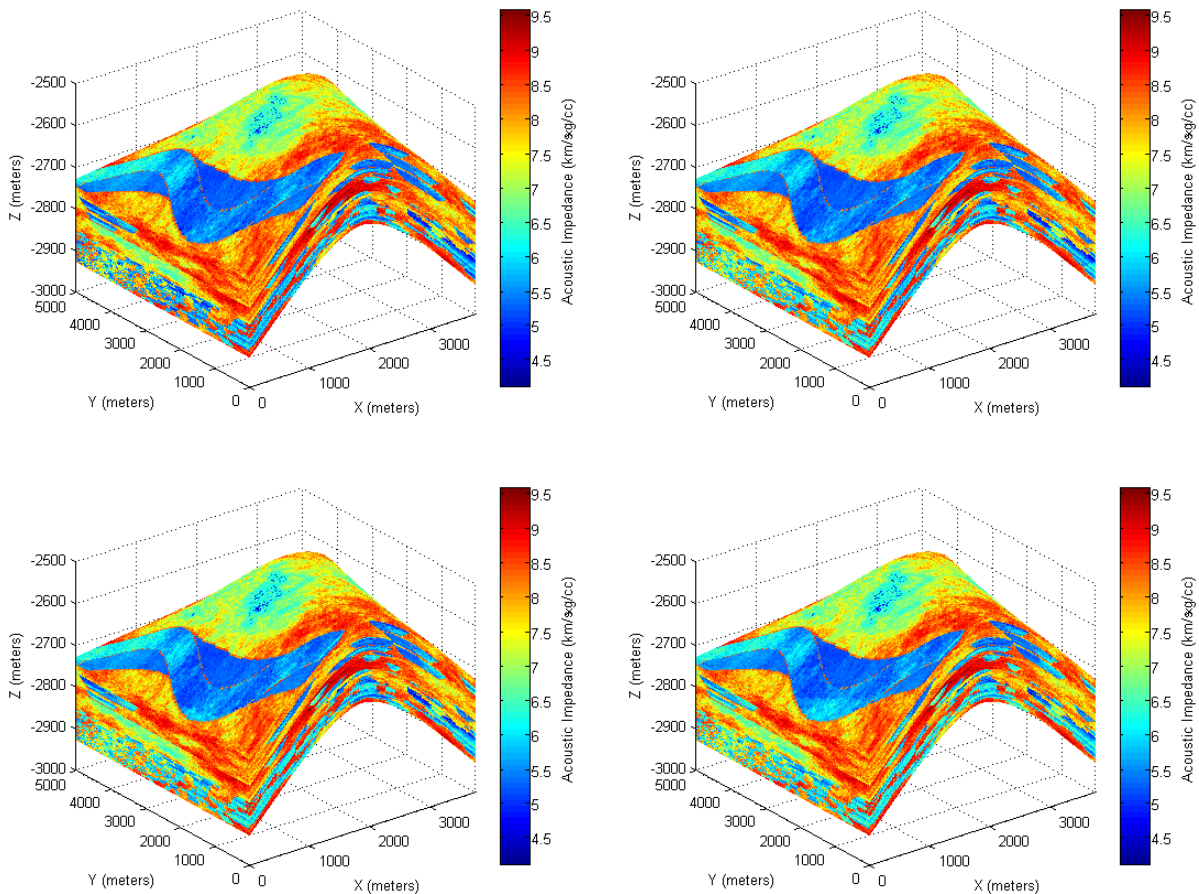


Figure 30. Acoustic impedance at the initial state (top-left) and 5 (top-right), 15 (bottom-left), and 30 (bottom-right) years after production. Color scales are matched.

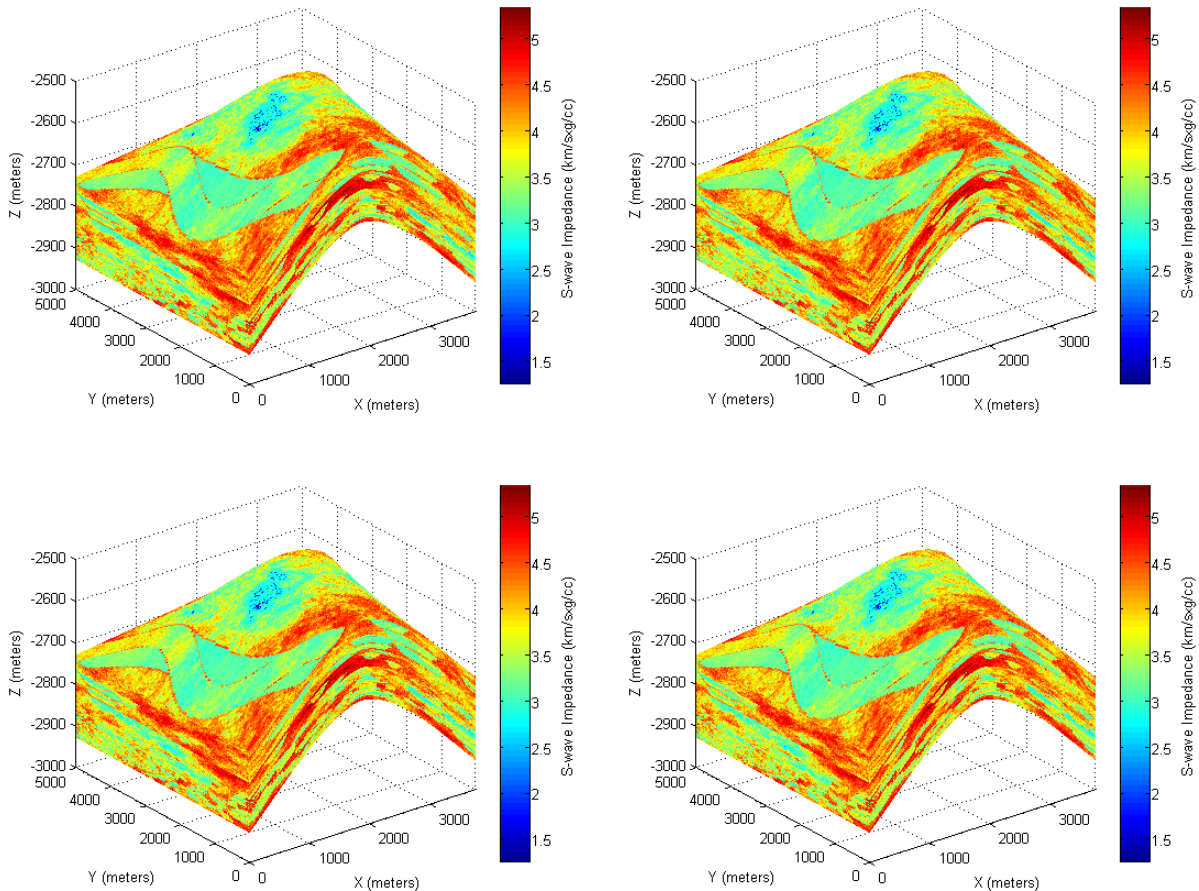


Figure 31. S-wave impedance at the initial state (top-left) and 5 (top-right), 15 (bottom-left), and 30 (bottom-right) years after production. Color scales are matched.

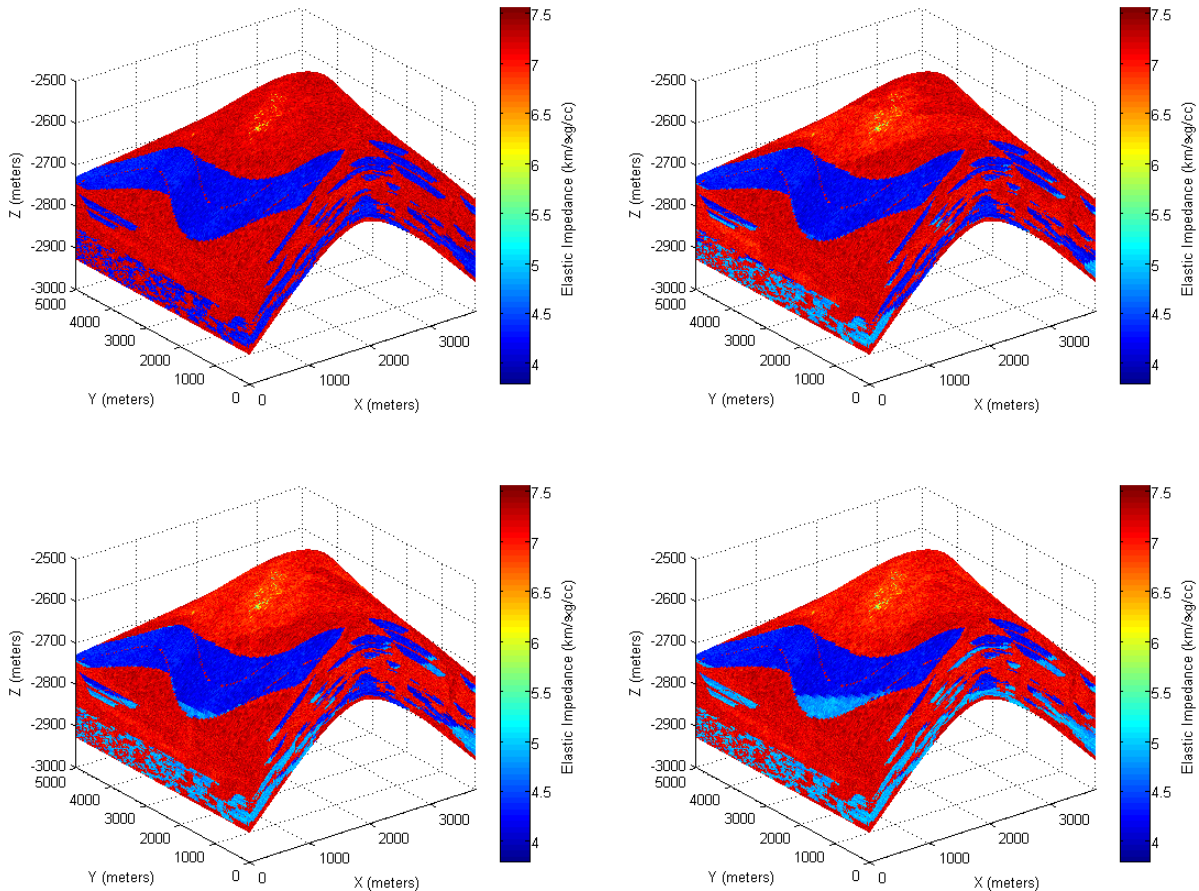


Figure 32. Elastic impedance at the initial state (top-left) and 5 (top-right), 15 (bottom-left), and 30 (bottom-right) years after production. Color scales are matched.

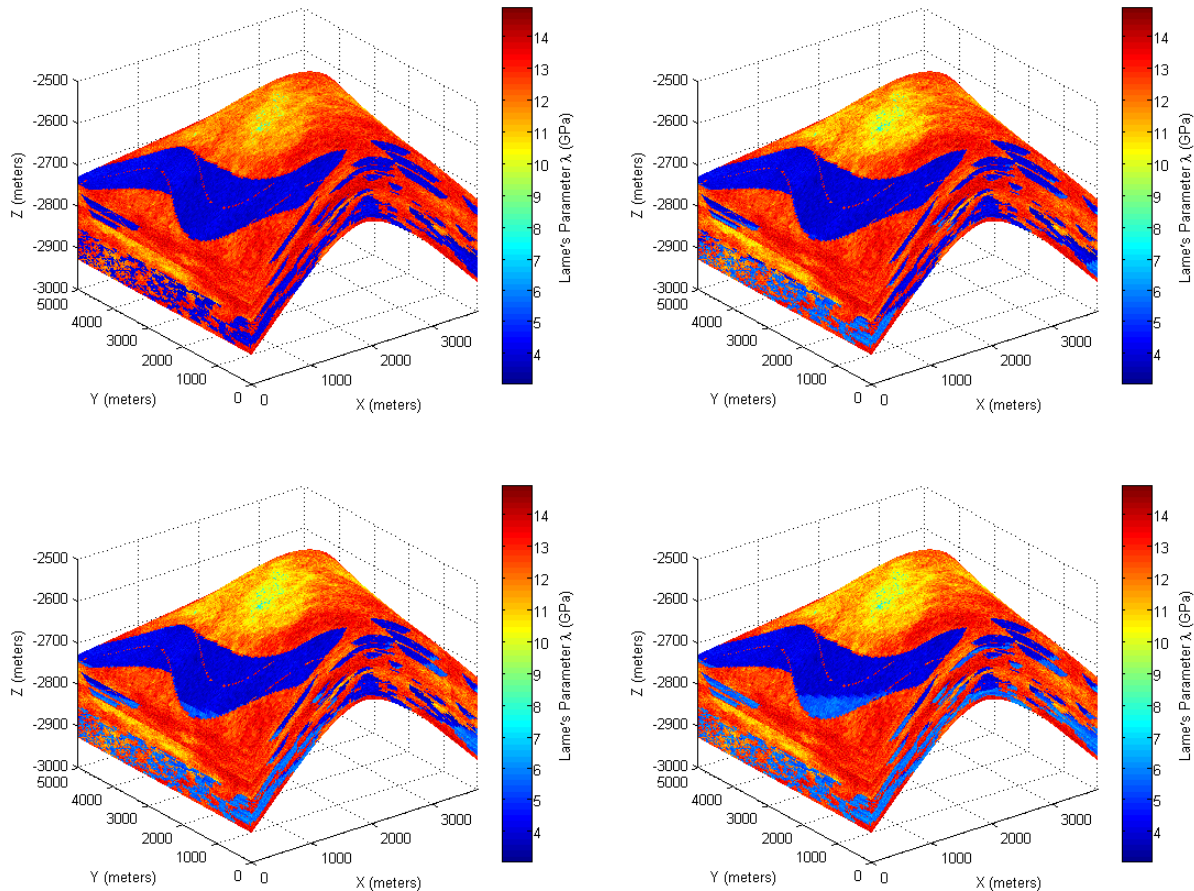


Figure 33. Lame's parameter λ at the initial state (top-left) and 5 (top-right), 15 (bottom-left), and 30 (bottom-right) years after production. Color scales are matched.

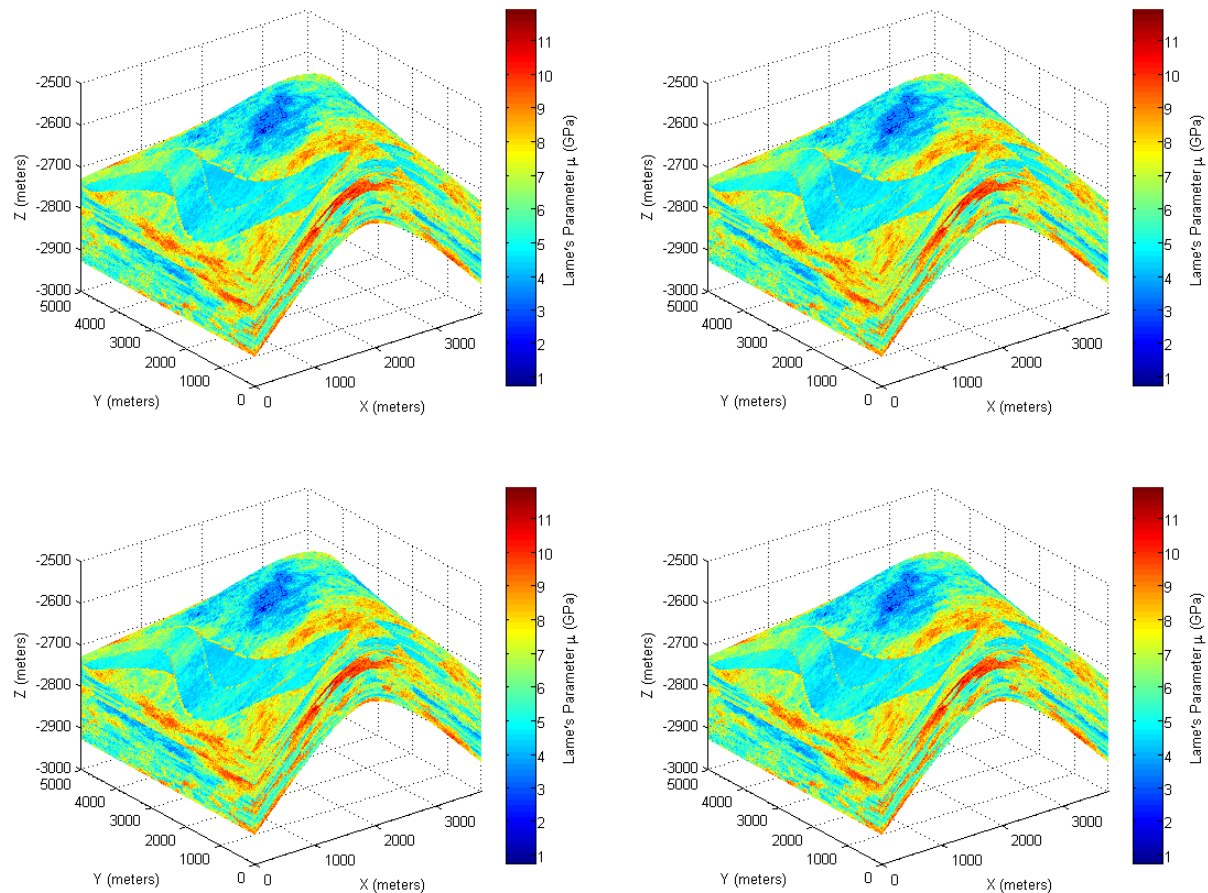


Figure 34. Lame's parameter μ at the initial state (top-left) and 5 (top-right), 15 (bottom-left), and 30 (bottom-right) years after production. Lame's parameter μ does not change during production.

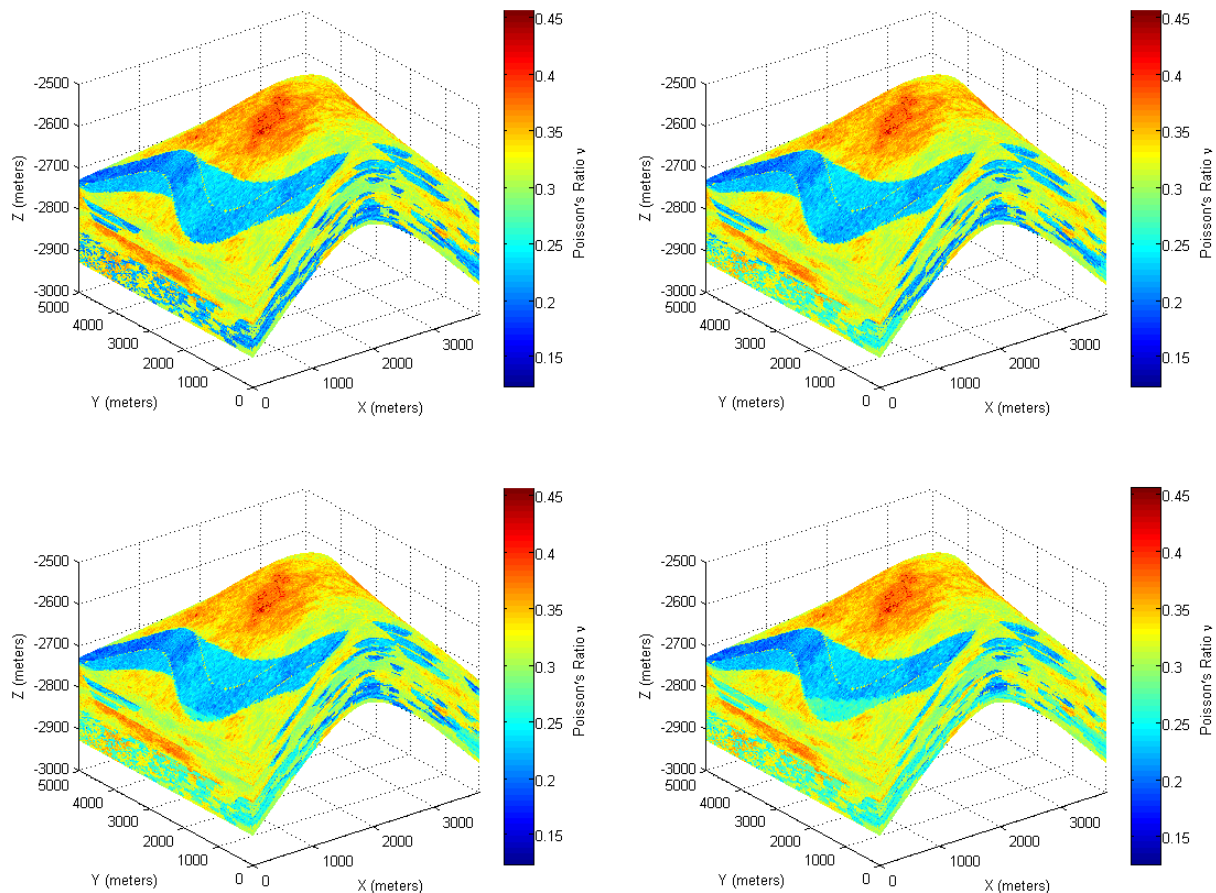


Figure 35. Poisson's ratio ν at the initial state (top-left) and 5 (top-right), 15 (bottom-left), and 30 (bottom-right) years after production. Color scales are matched.

Electrical Resistivity

Time-lapse electrical resistivity is also constructed based on the downscaled saturation obtained from the flow simulation. As mentioned before, 10% of random variability is added to the electrical resistivity for the initial state of the Stanford VI-E reservoir. Again, in order to create the Stanford VI-E as error-free data with natural variability, the given random variability should be maintained when computing the electrical resistivity at different times after oil production. The following equations are used to obtain the electrical resistivity of the rock with saturation condition 2 from the resistivity with initial saturation condition 1:

For the sand facies, the formation factor F is computed as:

$$F = \frac{R_{(1)}}{R_w S_{w(1)}^n} \quad (45)$$

where $R_{(1)}$ is the electrical resistivity of the rock with the brine saturation $S_{w(1)}$ and R_w is the brine electrical resistivity.

And the new electrical resistivity with the saturation condition 2 is obtained by the following equation:

$$R_{(2)} = F R_w S_{w(2)}^{-n} \quad (46)$$

where $R_{(2)}$ is the electrical resistivity of the rock with the brine saturation $S_{w(2)}$. This procedure is basically the Archie's law (1942) based on the assumption that the formation factor F , thus tortuosity and cementation, varies randomly but the saturation dependence of electrical resistivity does not change.

In case of shale facies, with the same assumption, the following procedure can be used based on the Waxman-Smits model (1968). The formation factor F is computed using the electrical resistivity with the saturation condition 1:

$$F = R_{(1)} \left(\sigma_w S_{w(1)}^n + B Q_v S_{w(1)}^{n-1} \right) \quad (47)$$

where σ_w are the brine electrical conductivity, B is the equivalent conductance of sodium clay exchange cations, and Q_v is the cation exchange capacity per unit pore volume. B and Q_v are obtained by the following equations:

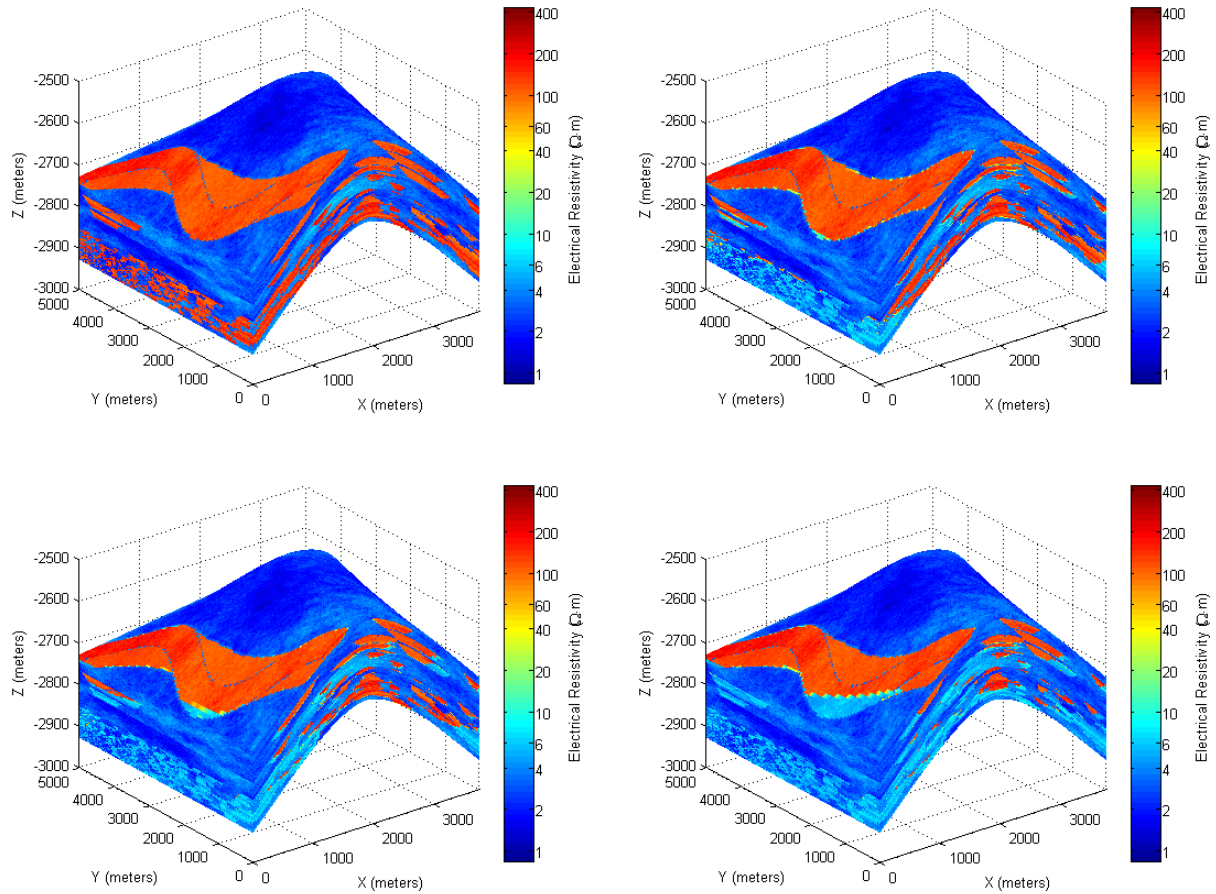


Figure 36. Electrical resistivity at the initial state (top-left) and 5 (top-right), 15 (bottom-left), and 30 (bottom-right) years after production. Color scales are matched.

$$B = 4.6 \left(1 - 0.6e^{-\sigma_w/1.3}\right), \quad Q_v = \frac{CEC(1-\phi)\rho_s}{\phi}$$

where CEC is the cation exchange capacity, ϕ is the porosity, ρ_s is the density of the solid phase in shale.

And then the electrical resistivity of shale with the saturation condition 2 is given by:

$$R_{(2)} = \frac{1}{\sigma_{(2)}} = 1 \left/ \left(\frac{\sigma_w S_{w(2)}^n}{F} + \frac{B Q_v S_{w(2)}^{n-1}}{F} \right) \right. \quad (48)$$

where $R_{(2)}$ and $\sigma_{(2)}$ are the electrical resistivity and conductivity of the rock with the brine saturation $S_{w(2)}$.

Figure 36 shows the electrical resistivity at initial state and 5, 15, and 30 years after production. As shown the figure, the electrical resistivity gives excellent contrast between the rocks saturated with different pore fluids.

Conclusions

A large-scale data set (6 million cells) named as the Stanford VI-E reservoir is generated with the purpose of testing any proposed algorithms for reservoir modeling, characterization, forecasting, and management.

Based on the original structure and stratigraphy of the Stanford VI (Catro et al., 2005) reservoir, the petrophysical properties and elastic attributes are created by using the improved rock physics models in the Stanford VI-E reservoir.

Due to the need of testing electromagnetic imaging algorithms, the well known empirical relations, Archie's method (1942) and Waxman-Smits model (1968) are applied to create electrical resistivity for sand and shale facies.

The complete and realistic two-phase flow simulation is performed for the situation that the sand and shale facies are saturated with different fluids. 30 years of oil production are simulated on an upscaled reservoir ($75 \times 100 \times 100 = 750,000$ cells) with an active aquifer below the reservoir. In order to make flow behavior and time-lapse data realistic, shale permeability is adjusted to more typical values. Also the net to gross value of pore volume is introduced in flow simulation to lead flow to occur mostly on channel.

From the change in saturation obtained by the flow simulation, the petrophysical properties, elastic attributes, and electrical resistivity are recomputed at different times during production. Random variability is carefully added to ensure that the Stanford VI-E reservoir is an error-free data set with natural variability.

Appendix

Dvorkin and Nur (1996) and Mavko et al. (2009) provide the statistical approximation of the rigorous solution of the contact cementation theory (Dvorkin et al., 1994), which is called the contact cement model. The equations are as follows:

$$K_{dry} = \frac{n(1-\phi_c)M_c S_n}{6} \quad (A.1)$$

$$G_{dry} = \frac{3K_{dry}}{5} + \frac{3n(1-\phi_c)G_c S_\tau}{20} \quad (A.2)$$

where n denotes the coordination number that is the average number of contacts per grain, ϕ_c represents the critical porosity above which the grains fall apart and become a suspension, and M_c and G_c are the P-wave modulus and shear modulus of the cement respectively.

The constants S_n and S_τ are given by the following equations:

$$S_n = A_n \alpha^2 + B_n \alpha + C_n$$

$$A_n = -0.024153 \Lambda_n^{-1.3646}, \quad B_n = 0.20405 \Lambda_n^{-0.89008}, \quad C_n = 0.00024649 \Lambda_n^{-1.9846}$$

$$S_\tau = A_\tau \alpha^2 + B_\tau \alpha + C_\tau$$

$$A_\tau = -10^{-2} (2.26\nu^2 + 2.07\nu + 2.3) \Lambda_\tau^{0.079\nu^2 + 0.1754\nu - 1.342}$$

$$B_\tau = (0.0573\nu^2 + 0.0937\nu + 0.202) \Lambda_\tau^{0.0274\nu^2 + 0.0529\nu - 0.8765}$$

$$C_\tau = 10^{-4} (9.654\nu^2 + 4.945\nu + 3.1) \Lambda_\tau^{0.01867\nu^2 + 0.4011\nu - 1.8186}$$

$$\Lambda_n = \frac{2G_c}{\pi G_s} \frac{(1-\nu_s)(1-\nu_c)}{1-2\nu_c}, \quad \Lambda_\tau = \frac{G_c}{\pi G_s}$$

$$\alpha = \left[\frac{2(\phi_c - \phi)}{3(1-\phi_c)} \right]^{1/2}$$

where G_s and ν_s are the shear modulus and the Poisson's ratio of the solid phase of the rock, G_c and ν_c are the shear modulus and the Poisson's ratio of the cement, and α is the ratio of the radius of the cement layer to the grain radius for the case that cement is deposited evenly on the grain surface, termed Scheme 2 by Dvorkin and Nur. (1996).

References

- Aki, K. and Richards, P. G., 1980, *Quantitative Seismology: Theory and Methods*, W.H. Freeman and Co., San Francisco, CA.
- Almeida, A. S. and Journel, A., 1994, "Joint simulation of multiple variables with a Markov-type coregionalization model": *Mathematical Geology*, 26, 565-588.
- Alumbaugh, D. L. and Morrison, H. F., 1995, "Theoretical and practical considerations for crosswell electromagnetic tomography assuming a cylindrical geometry": *Geophysics*, 60, 846-870.
- Archie, G. E., 1942, "The electrical resistivity log as an aid in determining some reservoir characteristics": *Transactions of the AIME*, 146, 54-62.
- Avseth, P., Dvorkin, J., and Mavko, G., 2000, "Rock physics diagnostic of North Sea sands: Link between microstructure and seismic properties": *Geophysical Research Letters*, 27, 2761-2764.
- Avseth, P., Mukerji, T., and Mavko, G., 2005, *Quantitative Seismic Interpretation: Applying Rock Physics Tools to Reduce Interpretation Risk*, Cambridge University Press, UK.
- Batzle, M. and Wang, Z, 1992, "Seismic properties of pore fluids": *Geophysics*, 57, 1396-1408.
- Bortfeld, R., 1961, "Approximation to the reflection and transmission coefficients of plane longitudinal and transverse waves": *Geophysical Prospecting*, 9, 485-502.
- Bourbié, T., Coussy, O., and Zinszner, B., 1987, *Acoustics of Porous Media*, Gulf Publishing Co., Houston, TX.
- Carman, P. C., 1937, "Fluid flow through granular beds": *Transactions of the Institute of Chemical Engineers*, 15, 150-166.
- Carroll, D., 1959, "Ion exchange in clays and other minerals": *Geological Society of America Bulletin*, 70, 749-780.
- Castagna, J.P., Batzle, M.L., and Eastwood, R.L., 1985, "Relationships between compressional-wave and shear-wave velocities in clastic silicate rocks": *Geophysics*, 50, 571-581.
- Castagna, J.P., Batzle, M.L., and Kan, T.K., 1993, "Rock physics -The link between rock properties and AVO response": in *Offset-Dependent Reflectivity - Theory and Practice of AVO Analysis*, J.P. Castagna and M. Backus, eds. *Investigations in Geophysics*, 8, Society of Exploration Geophysicists, Tulsa, Oklahoma, 135-171.
- Castro, S., Caers, J., and Mukerji, T., 2005, "The Stanford VI reservoir": 18th Annual Report, Stanford Center for Reservoir Forecasting, Stanford University, Stanford, CA.
- Clavier, C., Coates, G., and Dumanoir, J., 1984, "Theoretical and experimental bases for the dual-water model for interpretation of shaly sands": *SPE Journal*, 24, 153-168.
- Connolly, P., 1999, "Elastic impedance": *The Leading Edge*, 18, 438-452.
- Constable, S. and Cox, C. S., 1996, "Marine controlled source electromagnetic sounding 2. The PEGASUS experiment": *Journal of Geophysics Research*, 101, 5519-5530.
- Deutsch, C., 1989, "Calculating effective absolute permeability in sandstone/shale sequences": Paper SPE 17264.
- Dvorkin, J., Nur, A., and Yin, H., 1994, "Effective properties of cemented granular material": *Mechanics of Materials*, 18, 351-366.
- Dvorkin, J. and Nur, A., 1996, "Elasticity of high-porosity sandstones: Theory for two North Sea data sets": *Geophysics*, 61, 1363-1370.
- Gardner, G. H. F., Gardner, L. W., and Gregory, A. R., 1974, "Formation velocity and density – the diagnostic basics for stratigraphic traps": *Geophysics*, 39, 770-780.
- Gassmann, F., 1951. "Über die Elastizität poröser Medien": *Vier. der Natur. Gesellschaft in Zürich*, 96, 1-23.
- Goodway, B., Chen, T., and Downton, J., 1997, "Improved AVO fluid detection and lithology discrimination using

- Lame petrophysical parameters; $\lambda\rho$, $\mu\rho$, and λ/μ fluid stack, from P and S inversions": *CSEG national convention, Expanded Abstracts*, 148-151.
- Gray, D., Goodway, B., and Chen, T., 1999, "Bridging the gap: AVO to detect changes in fundamental elastic constants": *SEG Expanded Abstract*.
- Han, D. G., Nur, A., and Morgan, D., 1986, "Effects of porosity and clay content on wave velocities in sandstones": *Geophysics*, 51, 2093-2107.
- Hashin, Z. and Shtrikman, S., 1963, "A variational approach to the theory of the elastic behavior of multiphase materials": *Journal of the Mechanics and Physics of Solids*, 11, 127-140.
- Hill, R., 1952, "The elastic behavior of crystalline aggregate": *Proceeding of the Physical Society, London A*, 65, 349-354.
- Keller, G. V., 1987, "Rock and mineral properties": In *Electromagnetic Methods in Applied Geophysics*, Investigations in Geophysics Series 1, Society of Exploration Geophysics
- Knott, C. G., 1899, "Reflection and refraction of elastic waves, with seismological applications": *Phil. Mag., London*, 48(64-97), 567-569.
- Landrø, M., 2001, "Discrimination between pressure and fluid saturation changes from time-lapse seismic data": *Geophysics*, 66, 836-844.
- Lumley, D., Meadows, M., Cole, S., and Adams, D., 2003, "Estimation of reservoir pressure and saturations by crossplot inversion of 4D seismic attributes": *Expanded Abstracts*, 1513-1516.
- MacGregor, L., Sinha, M., and Constable, S., 2001, "Electrical resistivity structure of the Valu Fa Ridge, Lau Basin, from marine controlled-source electromagnetic sounding": *Geophysical Journal International*, 146, 217-236.
- Mao, S. and Journel, A., 1999, "Generation of a reference petrophysical/seismic data set: the Stanford V reservoir": 12th Annual Report, Stanford Center for Reservoir Forecasting, Stanford University.
- Mavko, G. and Nur, A., 1997, "The effect of a percolation threshold in the Kozeny-Carmen relation": *Geophysics*, 62, 1480-1482.
- Mavko, G., Mukerji, T., and Dvorkin, J., 2009, *The Rock Physics Handbook – Tools for Seismic Analysis of Porous Media*, Cambridge University Press, 2nd Edition, UK.
- Mukerji, T., Jørstad, A., Mavko, G., and Granli, J. R., 1998, "Near and far offset impedances: seismic attributes for identifying lithofacies and pore fluids": *Geophysical Research Letters*, 25, 4557-4560.
- Nebighian M. N.
- Poupon, A., and Leveaux, J., 1971, "Evaluation of water saturations in shaly formations": *Trans. Soc. Pro\$ Well Log Analysts*, 12th Annual Logging Symposium.
- Raymer, L. L., Hunt, E. R., and Gardner, J. S., 1980, "An improved sonic transit time-to-porosity transform": *Trans. Soc. Prof. Well Log Analysts*, 21st Annual Logging Symposium.
- Reuss, A., 1929, "Berechnung der Fliessgrenzen von Mischkristallen auf Grund der Plastizitätsbedingung für Einkristalle": *Z. Ang. Math. Meth.*, 9, 49-58.
- Shuey, R.T., 1985, "A simplification of Zoeppritz Equations": *Geophysics*, 50, 609-814.
- Simandoux, P., 1963, "Dielectric measurements on porous media: Application to the measurement of water saturations: Study of the behavior of argillaceous formations" *Revue de l'Institut Francais du Petrole*, 18, supplementary issue, 193-215.
- Strebelle, S., 2000, *Sequential Simulation Drawing Structures from Training Images*, Ph.D. thesis, Stanford University, Stanford, CA.
- Strebelle, S., 2002, "Conditional simulation of complex geological structures using multiple-point statistics":

Mathematical Geology, 34, 1-21

Tosaya, C. A. and Nur, A., 1982, "Effects of diagenesis and clays on compressional velocities in rocks": *Geophysical Research Letters*, 9, 5-8.

Tura, A. and Lumley, D., 1999, "Estimating pressure and saturation changes from time-lapse AVO data": *SEG Expanded Abstracts*, 1655-1658.

Voigt, W., 1928, *Lehrbuch der Kristallphysik*, Teubner, Leipzig

Waxman, M. H. and Smits, L. J. M., 1968, "Electrical conductivities in oil-bearing shaly sands": *SPE Journal*, 8, 107-122.

Wilt, M. J., Alumbaugh, D. L., Morrison, H. F., Becker, A., Lee, K. H., and Devez-Pan, M., 1995, "Crosshole electromagnetic tomography: Design considerations and field results": *Geophysics*, 60, 871-885.

Wyllie, M. R. J., Gregory, A. R., and Gardner, L. W., 1956, "Elastic wave velocities in heterogeneous and porous media": *Geophysics*, 21, 41-70.

Zoeppritz, K., 1919. "Erdbebenwellen VIIIB, Ueber Reflexion und Durchgang seismischer Wellen durch Unstetigkeitsflächen": *Goettlinger Nachrichten*, I, 66-84.